

A Near-Infrared and Optical Study of NGC 5822: An Open Cluster Hosting Barium-stars and Lithium-Enriched Giant Stars

N. Holanda,¹ ¹ V. Loaiza-Tacuri,^{1,2} A. Sonally,¹ S. Bijavara Seshashayana,^{3,4} M. P. Roriz,¹ C. F. Martinez,^{5,6} M. Borges Fernandes,¹ C. B. Pereira,¹ O. J. Katime Santrich,⁷ S. Daflon¹

¹Observatório Nacional, Rua General José Cristino 77, CEP 20921-400, São Cristóvão, Rio de Janeiro, RJ, Brazil

²Departamento de Física, Universidade Federal de Sergipe, Av. Marcelo Deda Chagas, S/N, 49107-230 São Cristóvão, SE, Brazil

³Materials Science and Applied Mathematics, Malmö University, 205 06 Malmö, Sweden

⁴Nordic Optical Telescope, Rambla José Ana Fernández Pérez, ES-38711 Breña Baja, Spain

⁵Universidad Nacional de Córdoba – Observatorio Astronómico de Córdoba, Laprida 854, X5000BGR, Córdoba, Argentina

⁶Consejo Nacional de Investigaciones Científicas y Técnicas (CONICET), Godoy Cruz 2290, CABA, CPC 1425FQB, Argentina

⁷Universidade Estadual de Santa Cruz, UESC, Rodovia Jorge Amado km 16, Ilhéus 45662000, Bahia, Brazil

Accepted XXX. Received YYY; in original form ZZZ

ABSTRACT

We present a chemical abundance study of giant stars in the Galactic open cluster NGC 5822, which hosts two barium stars (#002 and #201) and three lithium-enriched giants (#006, #102, and #240). Using high-resolution optical and near-infrared (*H* and *K* band) spectra from FEROS and IGRINS, we determine atmospheric parameters and abundances for 23 elements (Li, C, N, O, F, Na, Mg, Al, Si, P, S, K, Ca, Sc, Ti, Cr, Fe, Ni, Y, Ce, Nd, Yb, and Pb). This includes species not yet studied in this cluster, such as F, P, K, Yb, and Pb, as well as oxygen isotopic ratios $^{16}\text{O}/^{17}\text{O}$ and $^{16}\text{O}/^{18}\text{O}$. Membership was assessed using astrometry and chemical abundances, providing insight into the evolutionary stages of Li-enriched giants and cluster parameters (age, distance, extinction). However, the identification of Ba-stars remains challenging due to their binary nature and less reliable astrometric solutions. The cluster's abundances are broadly consistent with expectations for the Galactic thin disk. The mean fluorine abundance agrees with chemical evolution models predicting that young clusters (<2 Gyr) exhibit elevated [F/Fe], with production from SN II, SN Ia, AGB, and Wolf-Rayet stars. No distinct chemical or rotational features were found to explain the lithium enrichment, likely occurring either during the red clump phase or near the RGB tip. For the Ba-stars, nucleosynthesis models combined with the cluster's turn-off mass suggest polluting companion masses of 3.00 and $3.75 M_{\odot}$ for stars #002 and #201. These results highlight the importance of open clusters as laboratories for chemically peculiar stars.

Key words: techniques: spectroscopic – stars: abundances – stars: fundamental parameters – (Galaxy:) open clusters and associations: individual: NGC 5822

1 INTRODUCTION

Open clusters (OCs) are important benchmarks for studying stellar evolution and Galactic structure, as their member stars share common distances, initial chemical compositions, and ages. Moreover, age–chemical-clock relations, derived from empirical calibrations of stellar atmospheric abundances in OCs, provide critical insights into stellar ages and Galactocentric distances (e.g., Casali et al. 2019; Viscasillas Vázquez et al. 2022; Katime Santrich et al. 2022; Sales-Silva et al. 2022).

Although optical spectroscopy has traditionally been the standard for chemical abundance studies in OCs, near-infrared (NIR) spectroscopy has gained prominence due to its lower sensitivity to interstellar extinction and its access to molecular and atomic lines, which is particularly relevant for red giants and inaccessible in the optical

domain. The APOGEE survey (Majewski et al. 2017) has significantly advanced the chemical characterization of stars in OCs by providing high-quality NIR spectra. For instance, Donor et al. (2020) and Myers et al. (2022) used APOGEE DR16/17 data to analyze over 120 open clusters, tracing Galactic abundance gradients in 16 elements and investigating their evolution with age, thereby offering new insights into the Galaxy's chemical evolution. However, APOGEE is limited to the *H* band and offers a resolution of $R \sim 22,500$. Separately, Böcek Topcu et al. (2019, 2020) analyzed *H* and *K* band spectra of red giant stars in the OCs NGC 6940 and NGC 752, respectively, deriving abundances for 20 chemical species and offering a more comprehensive chemical characterization. Building on this approach, Holanda et al. (2024a) examined four stars in the young OC NGC 2345, including the determination of fluorine abundances. Beyond these efforts, Bijavara Seshashayana et al. (2024a,b) investigated fluorine abundances in OC stars to study chemical gradients and Galactic chemical evolution, also using high-resolution NIR spectroscopy; fluorine

* E-mail: nacizoholanda@on.br (NH)

Table 1. General information about the sample.

Star	RA [deg]	DEC [deg]	<i>V</i> [mag]	<i>K</i> [mag]	<i>G</i> [mag]	$G_{\text{BP}} - G_{\text{RP}}$ [mag]	π [mas]	μ_{α}^* [mas/yr]	μ_{δ} [mas/yr]	RUWE	Prob.
NGC 5822-001	226.0093	-54.3392	9.11	5.97	8.66	1.45	1.283	-7.348	-4.702	3.59	—
NGC 5822-002	225.9222	-54.3758	9.49	7.07	9.22	1.20	1.380	-7.751	-5.869	1.65	—
NGC 5822-006	226.0884	-54.3849	10.79	8.35	10.49	1.22	1.257	-7.555	-5.591	0.95	1.00
NGC 5822-008	226.1642	-54.3511	10.33	7.87	10.09	1.24	1.256	-7.641	-5.172	1.07	0.98
NGC 5822-102	225.9558	-54.3363	10.86	8.37	10.54	1.22	1.262	-7.495	-5.148	1.01	0.99
NGC 5822-201	225.9584	-54.2418	10.36	7.87	9.96	1.19	1.293	-6.809	-6.188	1.23	—
NGC 5822-224	225.8452	-54.4424	10.85	8.31	10.50	1.23	1.250	-7.886	-5.460	1.00	0.93
NGC 5822-240	226.1265	-54.5291	9.53	6.25	9.04	1.51	1.215	-7.605	-5.469	1.03	1.00
NGC 5822-316	226.1271	-54.5969	10.48	7.91	10.16	1.25	1.261	-7.540	-5.505	0.99	1.00
NGC 5822-348	225.7519	-54.4716	10.98	8.34	10.57	1.23	1.272	-7.572	-5.691	0.94	1.00
NGC 5822-375	225.8159	-54.2776	9.69	6.76	9.31	1.39	1.264	-7.542	-5.426	1.00	1.00
NGC 5822-443	225.7554	-54.2143	9.75	6.81	9.35	1.39	1.279	-7.465	-5.349	0.93	1.00
TYC 8681-389-1	226.0142	-54.0950	10.93	8.23	10.42	1.22	1.239	-7.441	-5.375	0.92	1.00

is only detectable via HF molecular lines in the *K* band. [Nandakumar et al. \(2022, 2023, 2024\)](#) conducted a series of investigations using high-resolution IGRINS spectra of 37 M giant stars, providing discussion on Galactic chemical evolution of phosphorus, fluorine, α -elements, and other species. These studies also emphasized the identification and analysis of previously neglected lines, particularly for heavy elements such as Y I and Ba I. Moreover, these works establish a key foundation in the literature and contribute to the validation of atomic and molecular line lists.

Parallel developments using NIR spectroscopy have focused in the study of the Galaxy's nuclear star cluster (NSC). Recent findings show that the NSC shares chemical similarities with the inner bulge, particularly in the enhanced α -element abundances of metal-rich stars (e.g., [Ryde et al. 2025](#)). These results suggest a shared chemical enrichment history and challenge models that invoke a recent dominant star formation burst in the NSC. Also recently, [Nandakumar et al. \(2025\)](#) performed a comprehensive chemical census of nine NSCs, identifying abundance trends consistent with those of the inner bulge population.

NGC 5822 is a well-studied OC in the optical domain, with several works investigating its red giant stars and providing chemical abundances for various species (e.g., [Pace et al. 2010](#); [Katime Sanrich et al. 2013b](#); [Sales Silva et al. 2014](#); [Peña Suárez et al. 2018](#); [Randich et al. 2022](#)). Among its main characteristics, we highlight its old age of 1.04 Gyr, distance of about 0.80 kpc, mean extinction in *V* band of 0.20 mag ([Hunt & Reffert 2023](#)), and mean metallicity of -0.09 ± 0.06 dex ([Peña Suárez et al. 2018](#)). However, no study to date has explored its red giants using NIR spectroscopy covering both the *H* and *K* bands. As a result, elements such as fluorine and ytterbium have never been investigated in the stars of this cluster. Moreover, the cluster NGC 5822 is also notable for hosting chemically peculiar stars: for instance, [Katime Sanrich et al. \(2013b\)](#) identified and analyzed two Ba-stars, #002 and #201. The authors cited that in the optical domain, these stars show strong Ba II lines with equivalent widths greater than 200 mÅ. These absorption features are found in the saturated regime of the curve-of-growth, preventing the derivation of reliable Ba abundances in these stars. Moreover, barium stars are exceptionally rare in OCs, and recent discussions on chemically peculiar cluster members have often centered on blue stragglers enriched in s-process elements (e.g., [Pal et al. 2024](#); [Nine et al. 2024](#)). In contrast, low-mass Li-rich giants account for only about 1% of all G-K giants (e.g., [Martell et al. 2021](#)). Notably, NGC 5822 hosts three giant stars with a significant degree of lithium enrichment (#006, #102, and #240). Unlike Ba-stars, the mechanism

responsible for lithium enrichment in giant atmospheres remains unclear and continues to be a topic of active investigation.

In this work, we present the most comprehensive chemical study to date of giant stars in the OC NGC 5822, combining high-resolution optical and NIR spectroscopy. We also perform a robust membership analysis to identify the true members of the cluster and better constrain evolutionary stages and the mean abundances of 23 chemical elements (Li, C, N, O, F, Na, Mg, Al, Si, P, S, K, Ca, Sc, Ti, Cr, Fe, Ni, Y, Ce, Nd, Yb, and Pb) and three isotopic ratios ($^{12}\text{C}/^{13}\text{C}$, $^{16}\text{O}/^{17}\text{O}$, and $^{16}\text{O}/^{18}\text{O}$), applied both chemically normal and peculiar stars associated with the cluster. Section 2 provides a general overview of the observational data and describes the membership and spectroscopic analyses. In Section 3, we present a detailed discussion of the derived abundances across different groups of elements, mixing models tests, and a particular approach on the nature of peculiar stars and nucleosynthesis models. Finally, Section 4 summarizes our main findings and presents the concluding remarks.

2 OBSERVATIONS AND ANALYSIS

The selected sample for this work is based on stars analyzed by [Peña Suárez et al. \(2018\)](#) (#001, #006, #008, #102, #224, #240, #316, #348, #375, #375, #443, and TYC 8681-389-1) and [Katime Sanrich et al. \(2013a\)](#) (#002 and #201). Our analysis combines public astrometric and photometric data with spectra obtained through a one observation proposal and an agreement between the Max Planck Institute/European Southern Observatory (ESO) and Observatório Nacional.

The publicly available data ([Gaia Collaboration et al. 2023](#)) were used for a comprehensive membership analysis of stars in the OC's direction, while the obtained spectra were used to derive detailed physical parameters and perform a chemical abundance analysis. The observations were carried out using the Immersion GRating INfrared Spectrometer (IGRINS; [Yuk et al. 2010](#)) on the 8.1 m Gemini South telescope at Cerro Pachón, Chile, by proposal submitted to Laboratório Nacional de Astrofísica (GS-2024A-Q-301; P.I. Nacizo Holanda). The IGRINS is a cross-dispersed NIR spectrograph with a resolving power of $R \approx 45,000$ that covers the *H* (14,900 - 18,000 Å) and *K* bands (19,600 - 24,600 Å), providing broad spectral coverage and high spectral resolution. The targets were observed using an ABBA nod sequence along the slit, employing exposure times to ensure spectra with a high signal-to-noise ratio, $S/\text{N}_{\text{IR}} \geq 150$, measured at 21,500 Å region. The data reduction process involved utilizing the IGRINS pipeline package, PLP. As part of the pipeline processing, the

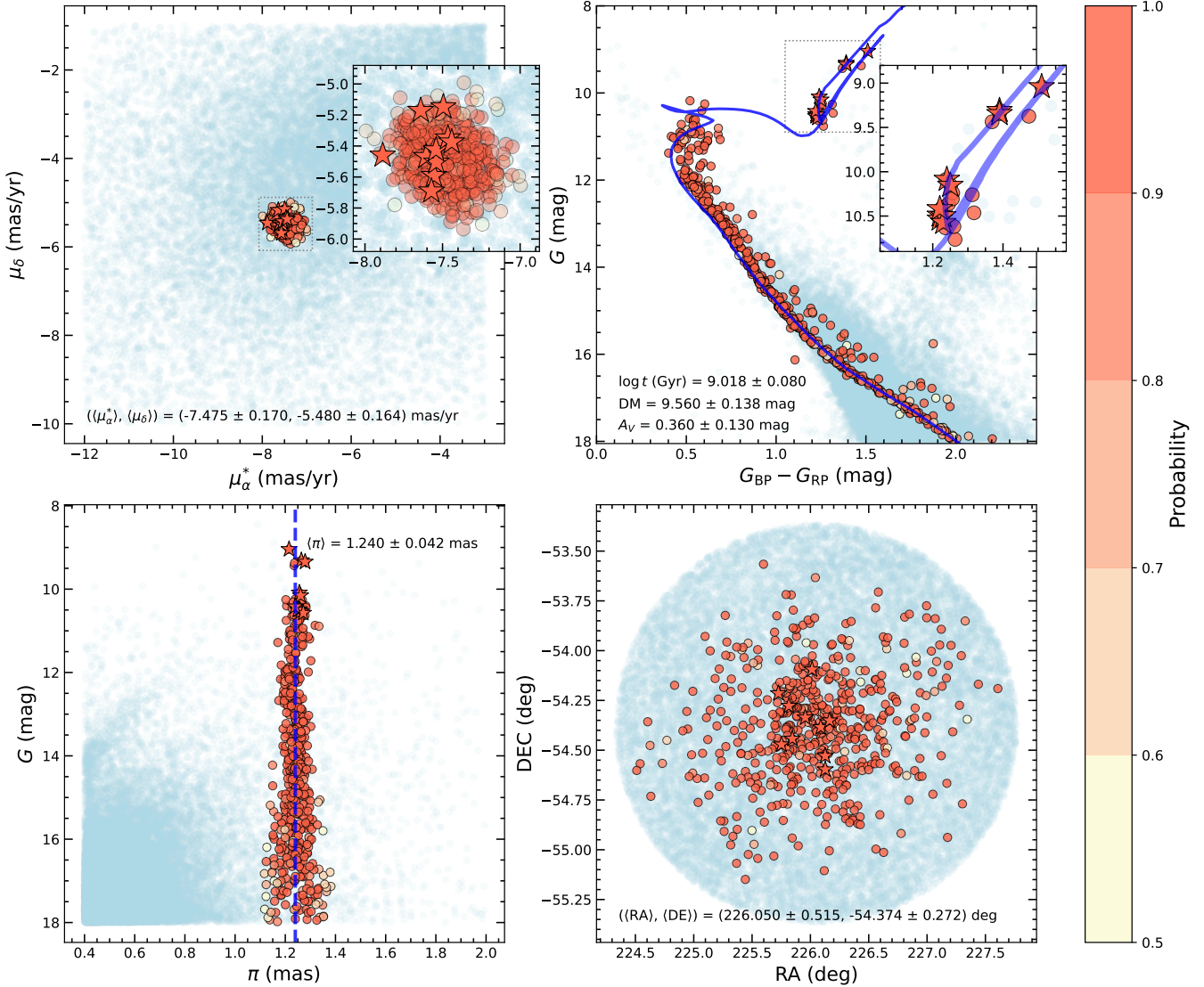


Figure 1. Proper motion distribution for bright stars around of the centre of NGC 5822 (top left), where the colour coded and light blue points (field contaminants) represent stars with probability to belonging to cluster of $P \geq 0.5$ and $0.0 \leq P < 0.5$, respectively. Colour–magnitude diagram (top right) is shown with an isochrone fitting (Bressan et al. 2012) for stars with proper motions and parallaxes characteristics of the cluster ($\log t = 9.018$).The bottom left panel shows magnitude versus parallax, where blue dashed line represents the mean parallax, while the bottom right panel represents the plane distribution of stars around the cluster. The stars analyzed in this work are marked with “star” symbols. Data were taken from Gaia Collaboration et al. (2023).

spectra were subjected to key steps such as telluric correction, wavelength calibration, and flat-field correction. Telluric features were corrected using observations of an A0V star acquired at a similar airmass to the target.

The second part of the observations were carried out using the Fiber-fed Extended Range Optical Spectrograph (Kaufer et al. 1999, FEROS;) at the 2.2 m Max Planck Gesellschaft/ESO Telescope in La Silla, Chile. The FEROS spectra have a resolving power of $R \approx 48,000$ within the spectral coverage of 3,600–9,200 Å. The exposure time were estimated to achieve a S/N_{OPT} high enough to resolve atomic and molecular lines. The FEROS Data Reduction System pipeline was used to reduce all optical spectra. The next subsections describes each dataset.

2.1 Membership analysis

To conduct a detailed study of the stars in NGC 5822, we identified all cluster members with $G \leq 18.0$ mag and determined key cluster parameters, including mean proper motion components (μ_α^*, μ_δ), parallax (π), distance (d), distance modulus ($M - m$), extinction (A_V), and age (t), based on data from *Gaia* DR3 (Gaia Collaboration et al. 2023). To achieve this, a zero-point offset correction was applied following Lindegren et al. (2021), and quality cuts were implemented to exclude unreliable and contaminated data. Stars with negative parallax, discrepant proper motion, and high Renormalized Unit Weight Error ($\text{RUWE} \geq 1.2$) were removed to mitigate the impact of poor astrometric solutions and unresolved binaries (e.g., Krolikowski et al. 2021; Hernandez et al. 2024).

Membership was determined using the Unsupervised Photometric Membership Assignment in Stellar Clusters code (UPMASK; Krone-

(Martins & Moitinho 2014), implemented via the Python-based pyUPMASK (Pera et al. 2021), which improves performance and usability over the original R version. Using three principal component analysis (PCA) dimensions, 10 outer loops, 25 maximum inner loops, and a minimum group size of 10 stars, we identified 557 likely members with astrometric probabilities ≥ 0.50 , including 10 giant stars from our spectroscopic sample (#006, #008, #102, #224, #240, #316, #348, #375, #443, and TYC 8681-389-1).

The threshold of $\text{RUWE} \geq 1.2$ includes stars such as #002 and #201, classified as Ba-stars by Katime Sanrich et al. (2013b). Ba-stars are chemically peculiar objects believed to form in binary systems (McClure 1983), typically through mass-transfer processes such as stellar wind accretion or Roche lobe overflow. As a result, their binary nature may have affected their astrometric solutions, potentially compromising the reliability of their membership probabilities. Additionally, #001 is not classified as a spectroscopic binary by Mermilliod et al. (2008) but exhibits a high RUWE value. Therefore, these three stars do not present probability determined. In Sec. 3, we present the chemical abundance results that can be linked with membership results. With the exception of neutron-capture elements, stars #002 and #201 show abundances consistent with the mean values observed for the OC. In contrast, star #001 presents discrepant abundance results in some cases when compared to other cluster members. Table 1 compile all basic information about the thirteen stars, including photometric and astrometric information from *Gaia* DR3 catalog, RUWE, and final astrometric probability obtained in the membership analysis.

For the isochrone fitting, we employed the routine available in the Automated Stellar Cluster Analysis code (AStECA; Perren et al. 2015), which uses a likelihood-based approach to achieve the best match between model isochrones and the observed stellar distribution. The stellar sample was defined using pyUPMASK, considering only stars with an astrometric membership probability ≥ 0.50 . Figure 1 shows the proper motion distribution for stars in NGC 5822 (top left), where the color scale represents the membership probability ($P \geq 0.5$). The top right panel presents the color-magnitude diagram (CMD) for stars that exhibit proper motion and parallax values consistent with cluster membership and field stars (in blue), along with the best-fit isochrone from Bressan et al. (2012), corresponding to $\log t = 9.018$.

The results obtained from the isochrone fitting are in excellent agreement with previous studies (Cantat-Gaudin et al. 2020; Dias et al. 2021; Hunt & Reffert 2023). The only significant discrepancy arises in the extinction value reported by Hunt & Reffert (2023), which differs from all other determinations for this OC. Table 2 presents the cluster parameters derived from isochrone fitting and from mean values based on the final list of member stars. For completeness, [Fe/H] results obtained from spectroscopic analysis are also provided.

2.2 Spectroscopic analysis

Spectroscopic analysis was performed using the radiative transfer code MOOG (version 2019; Sneden 1973), which serves as the primary tool for deriving atmospheric parameters and chemical abundances and assumes local thermodynamical equilibrium (LTE). The atmospheric parameters were determined using high-resolution FEROS spectra, which provide extensive spectral coverage, enabling the measurement of numerous absorption lines from neutral and singly ionized iron. The analysis was conducted using the grid of plane-parallel atmosphere models by Castelli & Kurucz (2004), which also assume LTE. IGRINS spectra were used to derive chemical abundances via spectral synthesis method, as described in the following subsections.

Table 2. Main cluster parameters. The values obtained in this work were calculated considering the mean values of the cluster members and assuming 8.34 ± 0.6 kpc for the solar galactocentric distance.

RA (deg)	226.050 ± 0.515	This Work
DEC (deg)	-54.374 ± 0.272	This Work
μ_{α}^* (mas yr $^{-1}$)	-7.475 ± 0.170	This Work
	-7.422 ± 0.222	Cantat-Gaudin et al. (2020)
	-7.417 ± 0.247	Dias et al. (2021)
	-7.462 ± 0.189	Hunt & Reffert (2023)
μ_{δ} (mas yr $^{-1}$)	-5.480 ± 0.164	This Work
	-5.534 ± 0.205	Cantat-Gaudin et al. (2020)
	-5.534 ± 0.209	Dias et al. (2021)
	-5.478 ± 0.179	Hunt & Reffert (2023)
π (mas)	1.240 ± 0.042	This Work
	1.187 ± 0.050	Cantat-Gaudin et al. (2020)
	1.188 ± 0.054	Dias et al. (2021)
	1.199 ± 0.048	Hunt & Reffert (2023)
R_{GC} (kpc)	7.72 ± 0.16	This Work
	7.69	Cantat-Gaudin et al. (2020)
[Fe/H]* (dex)	-0.06 ± 0.05	This Work
	-0.09 ± 0.06	Peña Suárez et al. (2018)
	+0.02	Randich et al. (2022)
$M_{\text{turn-off}}$ (M_{\odot})	2.05 ± 0.10	This Work
distance (pc)	817 ± 52	This Work
	854	Cantat-Gaudin et al. (2020)
	796 ± 27	Dias et al. (2021)
	808	Hunt & Reffert (2023)
$\log t$ (Gyr)	9.018 ± 0.080	This Work
	8.960	Cantat-Gaudin et al. (2020)
	9.039 ± 0.060	Dias et al. (2021)
	9.017	Hunt & Reffert (2023)
A_V (mag)	0.448 ± 0.056	This Work
	0.390	Cantat-Gaudin et al. (2020)
	0.481 ± 0.060	Dias et al. (2021)
	0.202	Hunt & Reffert (2023)
$M - m$ (mag)	9.516 ± 0.138	This Work
	9.660	Cantat-Gaudin et al. (2020)
	9.453	Hunt & Reffert (2023)

*The iron abundance was derived from spectroscopy.

2.2.1 Atmospheric parameters

First, the effective temperature (T_{eff}), surface gravity ($\log g$), microturbulent velocity (ξ_t), and metallicity ([Fe/H]), were derived using the standard spectroscopic approach. For that, we employed a carefully measured set of absorption lines from neutral and singly ionized iron (Fe I and Fe II), initially compiled by Lambert et al. (1996). While the original catalog contained 165 Fe I and 24 Fe II lines, a meticulous line-by-line evaluation was performed to select the most reliable measurements, utilizing Automatic Routine for line Equivalent widths in stellar Spectra (ARES v2; Sousa et al. 2015) and IRAF through the *splot* routine (Tody 1986). We imposed selection criteria of equivalent width between 10 mÅ to 150 mÅ with relative error of $\sigma_{\text{EW}} \leq 10\%$.

The parameter T_{eff} was determined by ensuring that the Fe I abundance showed no dependence on the excitation potential (χ). On the other hand, ξ_t was established by requiring that the Fe I abundance were independent of the reduced equivalent width (EW/λ). Surface gravity was calculated by enforcing ionization equilibrium, ensuring that $\log \varepsilon(\text{Fe I})$ is very similar to $\log \varepsilon(\text{Fe II})$. Table 3 presents final results for atmospheric parameters based on the standard spectroscopic analysis.

In addition, to derive a second and independent set of effective temperature values, we employed a photometric method based on the ($V - K$) color index, which is considered one of the most reliable

Table 3. Derived atmospheric parameters, metallicities, and rotational velocities for stars of the open cluster NGC 5822. The symbol “#” indicates the number of lines used to determine each set of spectroscopic parameters.

Star	$T_{\text{eff}}^{\text{V-K}}$ [K]	T_{eff} [K]	$\log g$ [cm s $^{-2}$]	ξ_t [km s $^{-1}$]	[Fe I/H] [dex]	#	[Fe II/H] [dex]	#	$v \sin i$ [km s $^{-1}$]	S/N _{OPT}	S/N _{IR}
NGC 5822-001	4415	4360	1.55	1.38	-0.12	52	-0.12	7	4.7	116	280
NGC 5822-002	5104	5170	2.65	1.65	-0.06	57	-0.06	9	5.8	200	360
NGC 5822-006	5079	5110	2.85	1.22	+0.00	65	+0.00	9	6.1	157	170
NGC 5822-008	5055	4990	2.70	1.31	-0.01	64	-0.01	12	5.0	167	230
NGC 5822-102	5021	5040	2.75	1.23	-0.09	65	-0.09	10	5.7	185	156
NGC 5822-201	5022	5150	2.60	1.44	-0.12	57	-0.12	11	4.7	140	250
NGC 5822-224	4983	5030	2.70	1.14	-0.03	64	-0.03	10	4.0	160	270
NGC 5822-240	4315	4410	1.90	1.43	-0.10	45	-0.10	10	3.0	210	255
NGC 5822-316	4929	5050	2.75	1.35	+0.00	63	+0.01	11	3.0	149	310
NGC 5822-348	4855	5030	2.80	1.29	-0.07	59	-0.07	12	2.8	132	222
NGC 5822-375	4581	4640	2.10	1.45	-0.09	49	-0.11	12	2.2	106	200
NGC 5822-443	4574	4670	2.30	1.55	-0.15	47	-0.15	10	2.8	128	237
TYC 8681-389-1	4793	5100	2.90	1.38	-0.02	43	-0.02	10	3.1	70	170

temperature indicators for giant stars (Alonso et al. 1999). For this calculation, we adopted the extinction ratio $A_V/E(V - K) = 1.13$ (Cox 2000, and references therein) and a color excess of $E(B - V) = 0.145$ mag, obtained from isochrone fitting. The observed mean difference ($T_{\text{eff}} - T_{\text{eff}}^{\text{V-K}}$) is 39 K, with a standard deviation of 82 K. The Pearson correlation coefficient between the two sets is +0.98, indicating a strong linear agreement between the spectroscopic and photometric temperatures, despite a small systematic offset.

2.2.2 Projected rotational velocities

Stellar rotation can be investigated through the projected rotational velocity ($v \sin i$) and is a powerful characteristic that can be related to chemical abundances for understanding internal structure. To estimate the possible contributions of rotational velocity in the chemical pattern of the peculiar stars analyzed here, we determined the $v \sin i$ by using spectral synthesis of the Fe I 5848 Å, 6027 Å, 6188 Å lines. Following the same methodology adopted in Holanda et al. (2021), we fixed macroturbulence velocity at 3.0 km s $^{-1}$, typical for G and K giants (Fekel 1997), and considering the instrumental broadening of the FEROS spectral resolution (FWHM ≈ 0.13). The best value of $v \sin i$ for each line was obtained using an iterative procedure until we find smallest deviation between the synthetic and observed spectra, and the mean value for each star is shown in Table 3.

2.2.3 Chemical abundance determination

The list of chemical species analyzed was primarily compiled based on the transitions available within the TGRINS spectral coverage. When possible, the same species were also analyzed in the FEROS data, and in such cases, we adopted the average abundance value derived from both optical and NIR spectra. The only exceptions are lithium and lead: Li was included due to its importance as a sensitive tracer of internal mixing and stellar evolutionary processes, and, Pb was included to represent the third peak of heavy elements, which is important to our study of chemical enrichment in Ba-stars (see Sec. 3.6.1).

We adopted two techniques to derive chemical abundances: equivalent width and spectral synthesis. Equivalent width measurements were performed in the optical for Na, Mg, Al, Si, Ca, Ti, Cr, Fe, Y, Ce, and Nd, while species such as Li, C, N, O, S, Sc, and Pb were analyzed using the spectral synthesis technique. On the other hand, all chemical abundances derived from the NIR region were obtained exclusively through spectral synthesis, since molecular bands are

ubiquitous along NIR wavelengths. The line lists used in this work are similar to those adopted by previous works of our group (see Holanda et al. 2024a, and references therein). We used the LINEMAKE program¹ (Placco et al. 2021, and references therein) to generate the input line lists for all spectral regions used in the synthesis, with minor adaptations applied when necessary.

Concerning the analysis of light species in optical spectra, carbon abundances were derived from the C₂ (0,1) band head of the Swan system at 5635 Å (Lambert 1978; Huber & Herzberg 1979), while nitrogen abundances were obtained from CN lines in the 8002–8005 Å range (Sneden & Lambert 1982). The wavelengths for ¹²CN and ¹³CN lines were adopted from Davis & Phillips (1963) and Wyller (1966), respectively. Due to telluric contamination affecting the [O I] 6300 Å line, oxygen abundances were determined from NIR analysis and adopted as fixed values in the optical analysis, given the interdependence of CNO species. Additionally, lithium abundances were determined from the Li I $\lambda 6708$ resonance doublet, assuming LTE conditions and accounting for nearby CN and Fe lines. Hyperfine and isotopic components of the Li line were included, with oscillator strengths and wavelengths taken from Smith et al. (1998) and Hobbs et al. (1999).

For the determination of light element abundances from NIR spectra, rotational-vibrational transitions of CO molecules were used to derive the abundances of ¹²C (Goorvitch 1994), as well as the isotopes ¹³C, ¹⁷O, and ¹⁸O, while OH molecular lines were adopted to determine the abundance of ¹⁶O (Brooke et al. 2016). The CO and OH lines are abundant in the NIR spectra of evolved stars, allowing us to analyze different regions in the *H* and *K* bands to obtain mean abundance values. However, the OH molecule has a low dissociation potential, making the synthesis process challenging for the higher temperature stars in our sample. Additionally, nitrogen abundances were determined by analyzing the electronic transitions of ¹²C¹⁴N ($A^2\Pi - X^2\Sigma$; Sneden et al. 2014).

To address the interdependence of these light species, we followed a procedure similar to that described by Smith et al. (2013), summarized as follows: first, the ¹⁶O abundance was constrained using OH lines and fixed to estimate the ¹²C abundance from the synthesis of ¹²CO lines. The derived ¹²C abundance was then used to refine the ¹⁶O abundance from OH lines, and this updated ¹⁶O value was subsequently fixed to obtain the final ¹²C abundance from ¹²CO lines. Finally, nitrogen abundances were determined through CN synthesis,

¹ Available at <https://github.com/vmplacco/linemake>

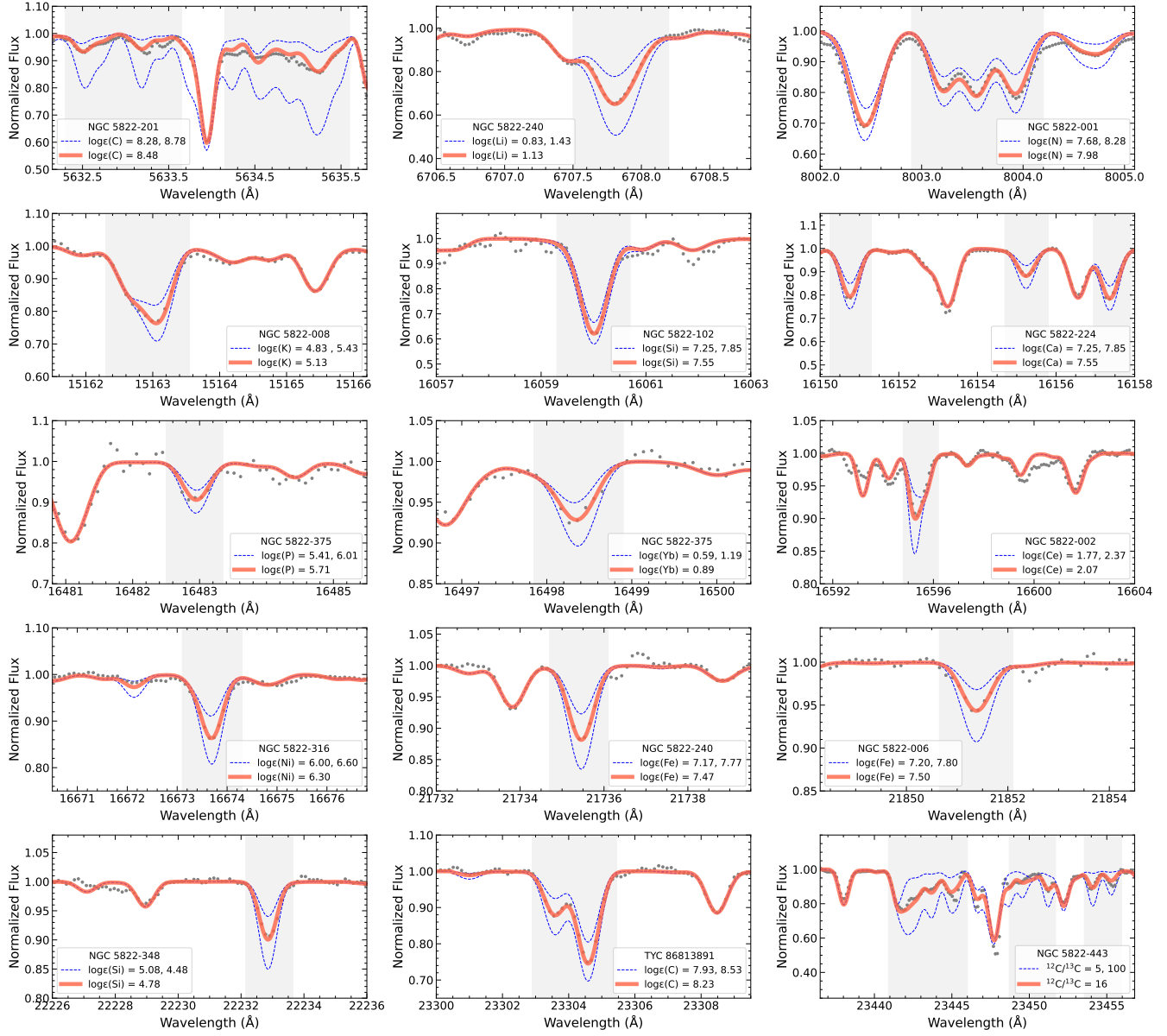


Figure 2. Examples of best-fitting results obtained from synthetic spectra (red lines) and observed IGRINS spectra (grey points) of stars. Additional lines are included to illustrate variations in abundance for the same spectral features (blue dashed-lines; do not represent uncertainties).

keeping the final ^{16}O and ^{12}C abundances fixed. Given that $\text{C}/\text{O} \leq 1.0$, the impact of CO and OH lines on nitrogen abundance is minimal. For these molecular species, we adopted dissociation energy values of $D_0(\text{CO}) = 11.092 \text{ eV}$, $D_0(\text{OH}) = 4.411 \text{ eV}$, and $D_0(\text{CN}) = 7.724 \text{ eV}$.

The isotopic ratios $^{12}\text{C}/^{13}\text{C}$ and $^{16}\text{O}/^{17,18}\text{O}$ were derived using gf -values from Kurucz (2011). The $^{12}\text{C}/^{13}\text{C}$ ratio was determined by analyzing two spectral regions containing the $^{13}\text{C}^{16}\text{O}$ (2–0) R49–56 and (3–1) R46–R57 lines. The $^{16}\text{O}/^{17}\text{O}$ ratio was obtained through spectral synthesis of two regions featuring the $^{12}\text{C}^{17}\text{O}$ (2–0) R28 and R29 lines. Additionally, the $^{16}\text{O}/^{18}\text{O}$ ratio was determined using the $^{12}\text{C}^{18}\text{O}$ (2–0) R23 line. In Section 2.2.4 we propagate the uncertainties of atmospheric parameters and CNO variation in these ratios, since oxygen isotopic ratios are very sensitive to atmospheric parameters.

The fluorine abundance was determined through analysis of the rotational-vibrational transitions of H^{19}F (1–0) R11 and R9, using

the gf -values from Jönsson et al. (2014). These lines, located at 23134 \AA and 23357 \AA , respectively, are commonly used in the literature to determine fluorine abundances in cool stars. However, their intensities decrease significantly with increasing temperature, a characteristic behavior of certain molecular absorption features ($D_0(\text{F}) = 5.869 \text{ eV}$).

Additionally, the chemical abundances of Na I , Mg I , Al I , Si I , P I , S I , K I , Ca I , Sc I , Ti I , Cr I , Fe I , Ni I , Ce II , Nd II , and Yb II were determined via NIR spectral synthesis of atomic lines. Much of the line information was sourced from Afşar et al. (2018), Civiš et al. (2013), Kramida et al. (2014), Pehlivan et al. (2015), Hasselquist et al. (2016), and Cunha et al. (2017). In Figure 2, we present examples of spectral synthesis performed in different regions of the optical and NIR spectra.

We have applied available corrections to the abundance values, considering the departure from LTE (NLTE) observed in late type

stars. In this sense, we employed correction grids provided by [Lind et al. \(2009\)](#) for Li I, [Lind et al. \(2011\)](#) for Na I, [Osorio et al. \(2015\)](#) for Mg I, [Nordlander & Lind \(2017\)](#) for Al I, [Mashonkina et al. \(2012\)](#), (private communication) for Pb lines.

Figure 3 compares our individual abundance results with distributions from the literature, based on various sources that employed similar spectroscopic analysis methods. All abundance ratios were normalized to the solar abundances of [Asplund et al. \(2009\)](#). Finally, all abundance results and isotopic ratios are shown in Table 4 and Table 5. These results will be discussed in detail in Section 3.

2.2.4 Abundance uncertainties

We provide an analysis of the uncertainties in determining the chemical abundances for the star #443, which serves as a representative example for our sample. This analysis follows the methodology described in [Holanda et al. \(2020b\)](#); in summary, the uncertainty in T_{eff} is derived from the error in the slope of the [Fe I/H] versus χ relation, while the uncertainty in ξ_t is estimated from the error in the slope of [Fe I/H] versus $\log \text{EW}/\lambda$. The uncertainty in surface gravity is determined iteratively by adjusting $\log g$ until the difference between the mean abundances of [Fe I/H] and [Fe II/H] equals the standard deviation of [Fe I/H].

These uncertainties in the atmospheric parameters are subsequently propagated to assess the overall uncertainties in the chemical abundances, which are listed in Table 6. The total abundance uncertainty, σ_{atm} , is computed as the square root of the sum of the squared uncertainties associated with the atmospheric parameters, i.e.:

$$\sigma_{\text{atm}}^2 = \sigma_{T_{\text{eff}}, \log \varepsilon(X)}^2 + \sigma_{\log g, \log \varepsilon(X)}^2 + \sigma_{\Delta \log \varepsilon(\text{Fe}), \log \varepsilon(X)}^2 + \sigma_{\xi_t, \log \varepsilon(X)}^2. \quad (1)$$

Table 7 presents the variations in the abundances of carbon, nitrogen, and oxygen. Additionally, the three columns in the table illustrate how an increase of 0.20 dex in the CNO abundances affects the results, due to the interdependence of these species. The total uncertainty in the CNO abundances, σ_{CNO} , is calculated as the square root of the sum of the squared uncertainties in the abundances:

$$\sigma_{\text{CNO}}^2 = \sigma_{\Delta \log \varepsilon(\text{C})}^2 + \sigma_{\Delta \log \varepsilon(\text{N})}^2 + \sigma_{\Delta \log \varepsilon(\text{O})}^2. \quad (2)$$

For the uncertainties in the isotopic ratios, we considered the variations caused by a +0.20 dex increase in the abundances of the CNO species. For instance, an increase in nitrogen abundance by +0.20 dex led to a variation of -0.10 dex in oxygen abundance. This variation in oxygen abundance was then propagated to estimate its impact on the isotopic ratios of $^{16}\text{O}/^{17,18}\text{O}$.

3 DISCUSSION

In Figure 3, we compare the stars analyzed in NGC 5822's field with literature samples from different contexts. Stars with high astrometric membership probability are shown in red, while those with no probability are represented by yellow symbols. Light blue circles correspond to literature samples, including clump giant stars from [Mishenina et al. \(2006\)](#), C, N, O, Na, Mg), cool giant stars from [Ryde et al. \(2020\)](#), F, K giant stars in the solar neighborhood from [Nandakumar et al. \(2022\)](#), P), K giants from [Montelius et al. \(2022\)](#), Yb), and giants ($\log g \leq 3.0$) from [Contursi et al. \(2024\)](#), Pb). We also include dwarf stars analyzed by [Lucertini et al. \(2022\)](#), S), [Bensby et al.](#)

(2014, Al, Si, Ca, Ti, Cr, Ni), [Battistini & Bensby \(2015\)](#), Sc), and [Battistini & Bensby \(2016\)](#), Y, Ce, Nd), selected with Age < 7.0 Gyr and TD/D < 0.5. The gray dashed lines indicate solar abundance values.

Figure 4 compares the chemical abundances derived from optical (light blue) and NIR (red) spectra for the giant stars of NGC 5822. For the elements for which NLTE corrections are available in the literature (Li, Na, Mg, Al, and Pb), NLTE values are indicated as triangles. Overall, optical and NIR measurements are consistent within the uncertainties for most species, with only a few elements showing differences between the two spectral regions. When determining the chemical pattern of the cluster, we adopt the NLTE abundances whenever available and use the mean values between the optical and NIR measurements to minimize possible wavelength-dependent biases and to increase the number of usable lines for each species.

Concerning differences within the same chemical species, the Al abundances derived from optical lines and from NIR lines in LTE show a significant difference. This occurs because lines in the NIR are more sensitive to NLTE effects and tend to overestimate the abundance in LTE. After applying the NLTE corrections to the NIR lines ([Nordlander & Lind 2017](#)), the resulting values are much closer to the optical results, indicating that the discrepancy was largely driven by NLTE effects. For Ca, the mean abundance from optical lines differs by 0.11 dex from the NIR values; the NIR Ca lines have higher excitation potentials and may probe different atmospheric layers, and they may also be more sensitive to NLTE departures, uncertainties in the $\log g f$ values, or continuum determination. Any combination of these effects could shift the NIR abundances relative to the optical ones.

3.1 Light elements

Light elements are excellent tracers of internal mixing events and their chemical abundances in red giant stars provide important insights into stellar evolutionary processes. Following the first dredge-up (1DUP) during the ascent of the red giant branch (RGB), a decrease in the ^{12}C abundance is typically observed, accompanied by increases in ^{13}C , N, and Na. Regarding oxygen isotopes, ^{16}O remains almost unaffected, while ^{17}O increases due to the sequence of reactions $^{16}\text{O}(\text{p}, \gamma)^{17}\text{F}(\beta^+)^{17}\text{O}$, until equilibrium is reached via $^{17}\text{O}(\text{p}, \alpha)^{14}\text{N}$. In contrast, ^{18}O decreases through the $^{14}\text{N}(\alpha, \gamma)^{18}\text{F}(\beta^+)^{18}\text{O}$ reaction chain. Additionally, lithium abundance drops significantly, as ^7Li becomes diluted in the deep convective envelope and is rapidly destroyed through proton capture, $^7\text{Li}(\text{p}, \alpha)^4\text{He}$, at temperatures exceeding 2.5×10^6 K.

The stars in our sample show good agreement with N and O abundance values from the literature (Figure 3). Regarding carbon abundance, a slight enrichment in ^{12}C is noticeable in the two Ba-stars, #002 and #201. As mentioned before, this peculiar class of stars forms in binary systems and has undergone polluted from an asymptotic giant branch (AGB) companion, which can also be enriched in ^{12}C ([Karakas & Lattanzio 2014](#); [Lugardo et al. 2023](#)).

3.1.1 The Li-enriched giants

So-called “Li-rich giant stars”, commonly defined as having lithium abundances of $\log \varepsilon(\text{Li}) \geq 1.5$ dex, comprise approximately 1% of all G-K giant stars (see, e.g., [Brown et al. 1989](#); [Kumar et al. 2011](#); [Holanda et al. 2020a,b, 2023, 2024b](#)). In our sample, three stars (#006, #102, and #240) exhibit slight Li enrichment, with $\log \varepsilon(\text{Li}) \gtrsim 1.30$ dex. Although these values fall just below the classical threshold, we classify them as Li-enriched given their

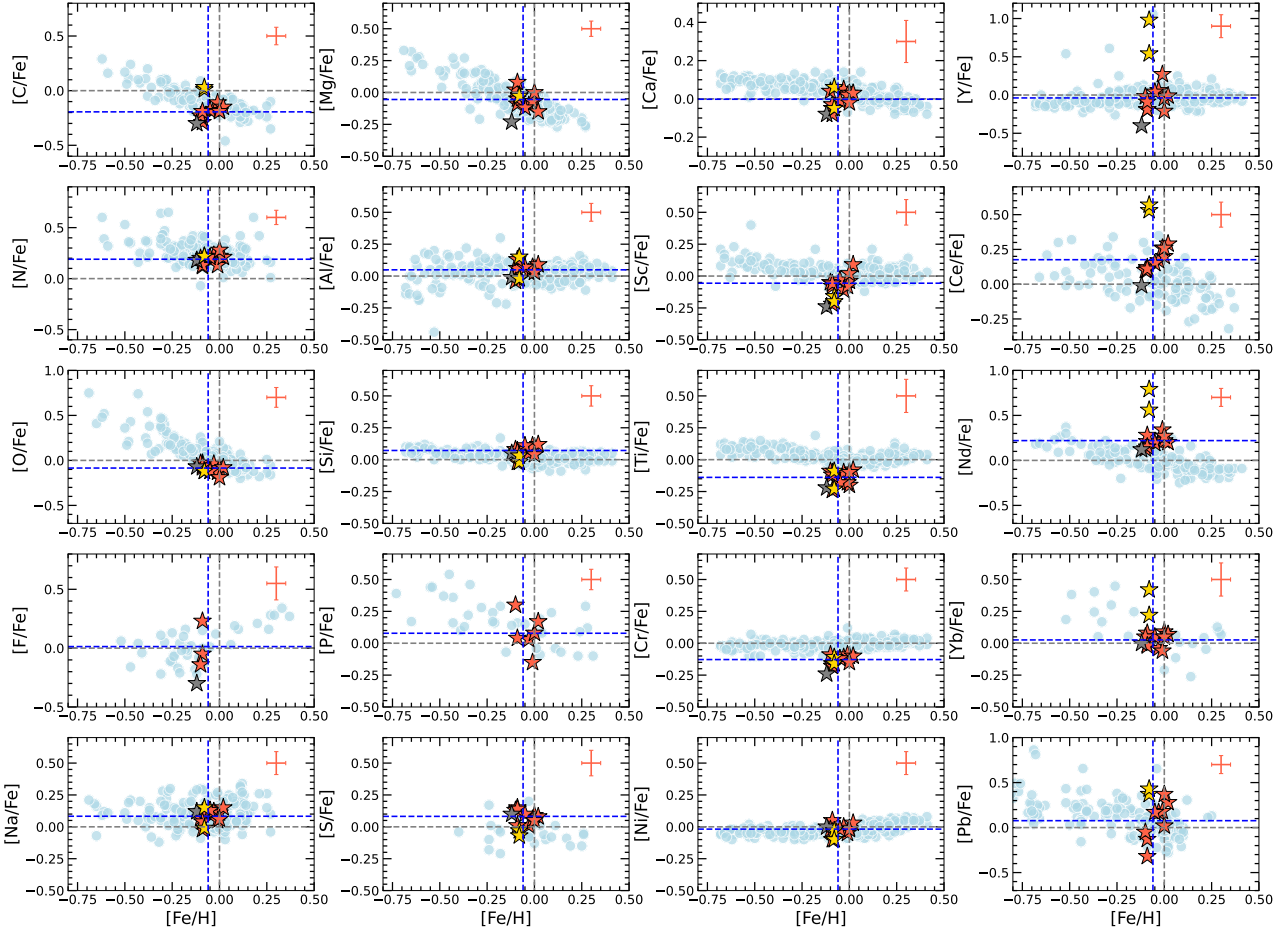


Figure 3. Abundance ratios $[X/Fe]$ versus $[Fe/H]$ for the analysed sample: stars with high astrometric probability are represented in red and the stars with low probability are denoted by yellow (#002 and #201; Ba-stars) and gray (#001) colour symbols. The light blue circles represent the samples of giant stars from Mishenina et al. (2006, C, N, O, Na, Mg), Ryde et al. (2020, F), Nandakumar et al. (2022, P), from Montelius et al. (2022, Yb), and from (Contursi et al. 2024, Pb). We also include dwarf stars analyzed by Lucertini et al. (2022, S), Bensby et al. (2014, Al, Si, Ca, Ti, Cr, Ni), Battistini & Bensby (2015, Sc), and Battistini & Bensby (2016, Y, Ce, Nd), selected with Age < 7.0 Gyr and TD/D < 0.5 . The gray dashed lines indicate the solar values, while the blue dashed lines represent the mean values of the cluster members.

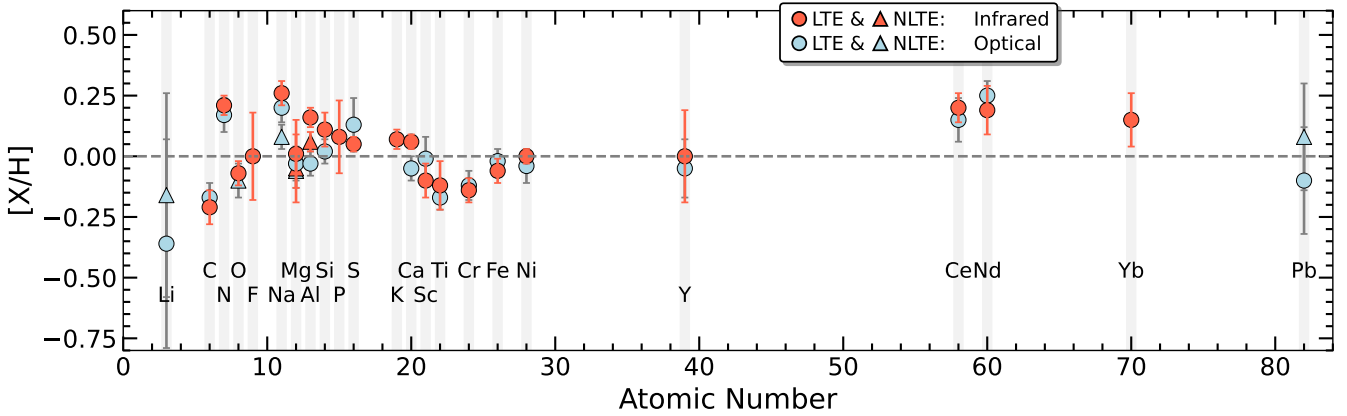


Figure 4. Mean elemental abundances for NGC 5822 derived from the optical (light blue) and NIR (red) spectral regions. Triangles indicate mean abundances corrected for NLTE effects. Abundance ratios are normalized to the solar abundances of Asplund et al. (2009).

Table 4. Abundance derived in this study. OC Mean indicates the mean cluster value, excluding the stars #001, #002, and #201.

$\log \varepsilon(X)$		#001	#002	#006	#008	#102	#201	#224	#240	#316	#348	#375	#443	TYC	OC Mean
Li I	OPT	-0.10	0.15	1.31	0.50	1.24	0.69	0.28	1.13	0.81	0.24	0.27	0.26	0.89	0.69 ± 0.43
Li I _{NLTE}	OPT	0.24	0.27	1.45	0.67	1.39	0.83	0.44	1.43	0.98	0.44	0.54	0.50	1.04	0.89 ± 0.42
C (CO)	IR	8.07	8.40	8.23	8.23	8.09	8.44	8.33	8.18	8.32	8.22	8.17	8.18	8.28	8.22 ± 0.07
C (C ₂)	OPT	8.18	8.48	8.28	8.26	8.18	8.48	8.30	8.17	8.23	8.27	8.23	8.30	8.20	8.26 ± 0.06
N (CN)	IR	8.07	8.03	8.09	8.07	8.04	8.07	7.98	7.97	8.07	8.03	8.07	7.99	8.07	8.04 ± 0.04
N (CN)	OPT	7.95	8.06	8.02	8.03	7.95	8.01	7.94	7.92	8.00	8.05	7.98	7.93	8.14	8.00 ± 0.07
O (OH)	IR	8.57	8.55	8.74	8.61	8.58	8.61	8.56	8.63	8.65	8.57	8.64	8.64	8.57	8.62 ± 0.05
O I _{NLTE}	OPT	8.66	8.59	8.56	8.58	8.63	8.53	8.56	8.69	8.57	8.57	8.67	8.62	8.43	8.59 ± 0.07
F (HF)	IR	4.26	—	—	—	—	—	—	4.51	—	—	4.42	4.79	—	4.57 ± 0.18
Na I	IR	6.50	6.43	6.53	6.54	6.47	6.46	6.52	6.47	6.50	6.59	6.41	6.51	6.45	6.50 ± 0.05
Na I	OPT	6.48	6.50	6.48	6.47	6.32	6.32	6.40	6.49	6.51	6.49	6.41	6.40	6.43	6.44 ± 0.06
Na I _{NLTE}	OPT	6.36	6.39	6.36	6.35	6.22	6.23	6.29	6.36	6.39	6.37	6.31	6.28	6.30	6.32 ± 0.05
Mg I _{NLTE}	IR	7.33	7.59	7.58	7.53	—	7.58	7.53	7.59	7.33	7.38	7.72	7.76	7.50	7.55 ± 0.14
Mg I	IR	7.43	7.67	7.64	7.60	—	7.66	7.61	7.70	7.39	7.44	7.73	7.85	7.56	7.61 ± 0.14
Mg I _{NLTE}	OPT	7.40	7.48	7.42	7.52	7.51	7.56	7.52	7.52	7.57	7.57	7.51	7.59	7.69	7.54 ± 0.07
Mg I	OPT	7.48	7.50	7.44	7.55	7.53	7.59	7.54	7.58	7.59	7.59	7.56	7.63	7.71	7.57 ± 0.07
Al I _{NLTE}	IR	6.44	6.60	6.48	6.52	6.43	6.43	6.52	6.51	6.54	6.52	6.41	6.58	6.48	6.51 ± 0.04
Al I	IR	6.60	6.75	6.60	6.64	6.57	6.58	6.65	6.64	6.66	6.63	6.57	6.57	6.59	6.61 ± 0.04
Al I	OPT	6.38	6.52	6.45	6.45	6.34	6.49	6.42	6.46	6.40	6.46	6.45	6.44	6.33	6.42 ± 0.05
Si I	IR	7.56	7.44	7.59	7.66	7.54	7.57	7.68	7.56	7.69	7.70	7.65	7.60	7.62	7.62 ± 0.07
Si I	OPT	7.56	7.53	7.53	7.56	7.44	7.51	7.55	7.60	7.57	7.54	7.52	7.53	7.48	7.53 ± 0.05
P I	IR	—	—	5.44	5.49	—	—	5.26	—	5.58	—	5.71	5.45	—	5.49 ± 0.15
S I	IR	7.11	7.06	7.11	7.15	7.15	7.05	7.14	7.17	7.20	7.21	7.18	7.19	7.16	7.17 ± 0.03
S I	OPT	7.33	7.12	7.15	7.27	7.10	7.10	7.22	7.37	7.19	7.22	7.32	7.47	7.17	7.25 ± 0.11
K I	IR	4.98	4.81	5.04	5.13	5.08	5.10	5.07	5.08	5.15	5.03	5.14	5.09	5.15	5.10 ± 0.04
Ca I	IR	6.29	6.42	6.41	6.41	6.36	6.32	6.39	6.38	6.44	6.41	6.44	6.36	6.39	6.40 ± 0.03
Ca I	OPT	6.22	6.38	6.37	6.32	6.22	6.25	6.32	6.24	6.30	6.24	6.32	6.15	6.25	6.29 ± 0.05
Sc I	IR	2.80	2.95	2.95	3.01	—	2.88	3.03	3.02	3.19	3.12	3.05	3.02	3.10	3.05 ± 0.07
Sc II	OPT	3.02	3.03	3.13	3.20	2.93	3.06	3.11	3.11	3.28	3.11	3.15	3.16	3.23	3.14 ± 0.09
Ti I	IR	4.85	4.80	4.82	4.72	4.68	4.67	4.75	4.96	4.87	4.78	4.89	4.93	4.91	4.83 ± 0.10
Ti I	OPT	4.60	4.91	4.87	4.77	4.74	4.76	4.78	4.73	4.86	4.76	4.79	4.73	4.79	4.78 ± 0.05
Cr I	IR	5.39	5.49	5.49	5.53	5.41	5.43	5.49	5.44	5.52	5.51	5.55	5.50	5.55	5.50 ± 0.05
Cr I	OPT	5.40	5.56	5.56	5.54	5.50	5.50	5.60	5.51	5.56	5.53	5.55	5.41	5.43	5.52 ± 0.06
Fe I	IR	7.38	7.39	7.44	7.51	7.41	7.45	7.50	7.41	7.52	7.47	7.41	7.47	7.51	7.44 ± 0.05
Fe I	OPT	7.38	7.44	7.50	7.49	7.41	7.38	7.47	7.40	7.50	7.43	7.41	7.35	7.48	7.44 ± 0.05
Fe II	OPT	7.39	6.20	7.50	7.49	7.41	7.38	7.47	7.40	7.51	7.43	7.39	7.35	7.48	7.44 ± 0.05
Ni I	IR	6.19	6.18	6.24	6.22	6.17	6.12	6.17	6.21	6.26	6.26	6.21	6.21	6.23	6.22 ± 0.03
Ni I	OPT	6.24	6.20	6.20	6.07	6.11	6.16	6.32	6.24	6.14	6.19	6.12	6.16	6.18	6.07 ± 0.07
Y I	IR	1.81	2.82	2.29	2.16	—	3.17	2.56	1.96	2.24	—	2.12	2.13	—	2.21 ± 0.19
Y II	OPT	1.80	2.67	2.24	2.18	2.02	3.21	2.39	2.10	2.15	2.14	2.25	2.10	2.00	2.16 ± 0.12
Ce II	IR	1.54	2.06	1.80	1.79	1.72	2.15	1.83	1.72	1.88	1.77	1.69	1.75	1.84	1.78 ± 0.06
Ce II	OPT	1.59	2.15	1.69	1.77	1.63	2.14	1.84	1.68	1.85	1.69	1.66	1.64	1.83	1.73 ± 0.09
Nd II	IR	1.47	2.15	1.52	1.59	1.62	2.02	1.77	1.65	1.54	1.58	1.46	1.56	1.77	1.61 ± 0.10
Nd II	OPT	1.61	2.27	1.73	1.69	1.64	1.94	1.75	1.75	1.69	1.61	1.63	1.58	1.60	1.67 ± 0.06
Yb II	IR	0.84	1.06	0.97	0.93	0.92	1.26	0.92	0.83	0.91	0.89	0.89	0.82	0.88	0.90 ± 0.05
Pb I	OPT	—	1.95	1.75	1.60	1.45	2.00	1.75	1.25	1.85	1.75	1.50	—	1.95	1.65 ± 0.22
Pb I _{NLTE}	OPT	—	2.12	1.92	1.77	1.62	2.18	1.93	1.43	2.03	1.92	1.70	—	2.12	1.83 ± 0.22

Table 5. Isotopic ratios derived in this study. OC Mean indicates the mean cluster value, excluding the stars #001, #002, and #201.

Isotopic ratio	#001	#002	#006	#008	#102	#201	#224	#240	#316	#348	#375	#443	TYC	OC Mean
¹² C/ ¹³ C(¹³ CO)	24	12	20	14	12	24	24	25	22	20	21	16	14	19 ± 5
¹⁶ O/ ¹⁷ O(¹⁷ O)	300	—	—	—	—	—	250	—	—	250	150	—	—	216 ± 58
¹⁶ O/ ¹⁸ O(¹⁸ O)	400	—	—	—	—	—	600	—	800	—	400	—	—	600 ± 200

marginally elevated abundances and typical measurement uncertainties ($\sigma_{\log \varepsilon(\text{Li})} \sim 0.20 \text{ dex}$).

Beyond lithium abundance, we investigated other potential anomalies in stellar activity, isotopic ratios and projected rotational velocities. As stars evolve off the main sequence, their magnetic activity decays; thus, no significant activity signatures are generally expected (e.g. [Wilson & Skumanich 1964](#); [Skumanich 1972](#)). However, two Li-enriched giants in our sample (#006 and #102) display Ca II H & K

emission (Figure 5), a classical indicator of chromospheric activity. These stars also show the highest $v \sin i$ values in the sample, 6.1 and 5.7 km s⁻¹. Rapid rotation combined with chromospheric activity in evolved stars is often associated with binarity, where a companion can induce spin-up and internal mixing ([Fekel et al. 2002](#); [Morel et al. 2004](#); [Fekel & Henry 2005](#)). However, no known companion explains the observed activity.

Previous studies have explored possible correlations between

Table 6. Abundance uncertainties for the star #443. From the second to the fifth column, we show the variations in abundances caused by the uncertainties in the atmospheric parameters. In the last column, we present the total uncertainty.

$\log \epsilon(X)$	ΔT_{eff}	$\Delta \log g$	$\Delta \xi_t$	$\Delta \log \epsilon(\text{Fe})$	σ_{atm}
	+80 K	+0.20 dex	+0.08 km/s	+0.10 dex	
Li I	+0.13	-0.08	-0.10	0.00	0.18
F (HF)	+0.12	+0.02	+0.01	+0.04	0.13
Na I	+0.06	-0.01	-0.03	-0.03	0.07
Mg I	+0.02	-0.01	-0.02	-0.02	0.04
Al I	+0.04	-0.02	-0.02	-0.02	0.05
Si I	-0.04	+0.02	-0.03	-0.02	0.06
P I	+0.02	+0.05	-0.03	0.00	0.06
S I	-0.09	-0.02	-0.02	-0.01	0.09
K I	+0.05	+0.01	-0.07	+0.04	0.10
Ca I	+0.07	-0.02	-0.05	-0.05	0.10
Sc II	-0.01	+0.09	-0.01	0.00	0.09
Ti I	+0.11	+0.01	-0.03	-0.03	0.12
Cr I	+0.07	0.00	-0.02	-0.02	0.08
Fe I	+0.03	+0.01	-0.04	+0.01	0.05
Ni I	+0.03	+0.03	-0.05	-0.04	0.08
Y II	-0.01	+0.06	-0.09	-0.09	0.14
Ce II	0.00	+0.07	-0.02	-0.02	0.08
Nd II	+0.02	+0.07	-0.04	-0.04	0.09
Yb II	+0.04	+0.11	0.00	0.00	0.12
Pb I	+0.05	-0.05	-0.05	0.00	0.09

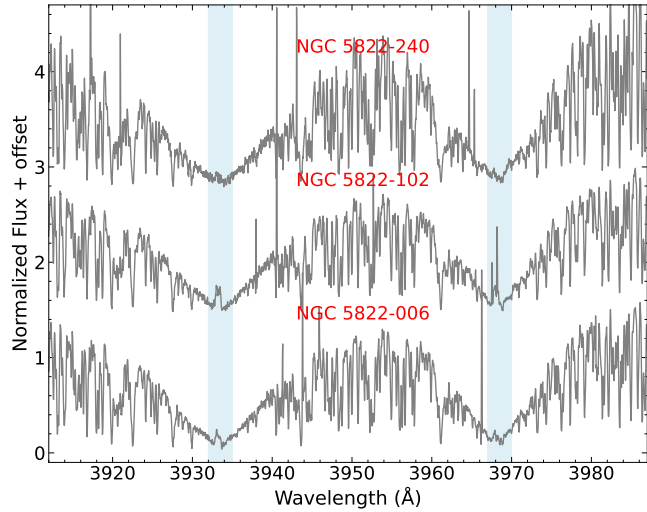


Figure 5. Normalized Ca II H & K spectra of the three Li-enriched giants in NGC 5822.

lithium abundance and chromospheric activity (e.g., Gonçalves et al. 2020; Xing et al. 2021; Sneden et al. 2022), as well as with rotation (e.g. Rebolo & Beckman 1988; Chaboyer et al. 1998; Drake et al. 2002; Magrini et al. 2021; Flauhabe et al. 2025). Some of these works suggest that stronger chromospheric flux and faster rotation may favor higher Li abundances. In our case, however, the measured $v \sin i$ values remain below the $\sim 8\text{--}10 \text{ km s}^{-1}$ threshold traditionally used to classify rapid rotators in this context (Drake et al. 2002).

Recently, Rolo et al. (2024) investigated the relation between lithium enrichment, stellar activity, and radial velocity (RV) variability in OC giants, including NGC 5822. Their Table 4 shows moderate correlations between RV and activity indicators (BIS, FWHM, and H α) for the star #102, together with a relatively high projected ro-

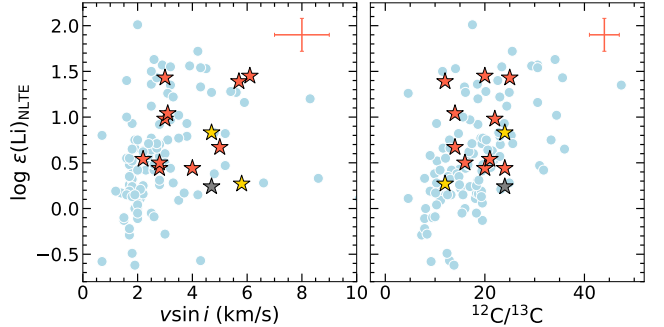


Figure 6. Lithium abundance as a function of projected rotational velocity and carbon isotopic ratio for giant stars. Open cluster members are shown in red, while stars with low membership probability are represented by yellow (#002 and #201; Ba stars) and gray (#001) symbols. G-K type giant stars analyzed by Takeda et al. (2019) and Takeda & Tajitsu (2017) are shown in light blue.

tational velocity. However, these correlations are based on a limited number of observations and are not supported by common periodicities in the RV and activity time series. On the other hand, the star #240 does not show significant RV-activity correlations. Taken together, these results do not provide sufficient evidence to establish a link between stellar activity and Li-enrichment in these stars.

Figure 6 shows lithium abundances, $v \sin i$, and $^{12}\text{C}/^{13}\text{C}$ for a sample of G-K giants from Takeda & Tajitsu (2017) and Takeda et al. (2019), compared with the thirteen giants analyzed here. The Li-enriched giants are broadly scattered in Figure 6 (left panel), showing no consistent trend linking higher Li abundance to higher $v \sin i$ values. Some Li-rich giants exhibit both low and moderate $v \sin i$, indicating that rotation alone cannot explain Li enrichment.

The surface carbon isotopic ratio $^{12}\text{C}/^{13}\text{C}$ provides a key diagnostic of extra mixing. However, lithium abundance does not correlate systematically with $^{12}\text{C}/^{13}\text{C}$ (Figure 6, right panel). Stars with elevated Li abundances appear across the full isotopic range, implying that deep mixing, typically associated with lower ratios, is not the unique mechanism responsible for Li enhancement. A notable case is the star #102, which exhibits a low $^{12}\text{C}/^{13}\text{C}$ ratio of 12, making it a candidate for having experienced additional mixing. Altogether, these results reinforce the view that Li-rich giants constitute a heterogeneous class of chemically peculiar stars, likely shaped by multiple or combined enrichment mechanisms.

Table 8 presents a comparison of the $v \sin i$ and $\log \epsilon(\text{Li})_{\text{NLTE}}$ values obtained in this work with those reported by Delgado Mena et al. (2016) and Tsantaki et al. (2023). A clear and systematic difference is observed between our measurements and those of Delgado Mena et al. (2016) for both $v \sin i$ and Li abundances in the NGC 5822 members. We highlight three key points in this first comparison: (1) Our $v \sin i$ values are consistently higher by $\sim 0.3\text{--}1.2 \text{ km s}^{-1}$, which may be attributed to differences in the macroturbulence values assumed; (2) Li abundances show a uniform offset of $\sim 0.1\text{--}0.3 \text{ dex}$, with the values from Delgado Mena et al. (2016) being systematically larger, probably due to discrepancies in the assumed atmospheric parameters by them; and (3) The relative star-to-star trends are preserved (for instance, #102 maintains the highest rotation and Li abundance in both studies). Delgado Mena et al. (2016) report a $T_{\text{eff}} = 5252 \text{ K}$ for star #102, i.e., 221 K higher than the value found in this work, which may explain the observed difference in Li abundance since this species is easily affected by effective temperature (see

Table 7. Influence of the errors in atmospheric parameters on the abundances of carbon, nitrogen, and oxygen and isotopic ratios for NGC 5822-443. We also show the dependence of the CNO abundance uncertainty on each light element.

$\log \varepsilon(X)$	ΔT_{eff}	$\Delta \log g$	$\Delta \xi_t$	$\Delta \log \varepsilon(\text{Fe})$	$\Delta \log \varepsilon(\text{C})$	$\Delta \log \varepsilon(\text{N})$	$\Delta \log \varepsilon(\text{O})$	σ_{atm}	σ_{CNO}
$\text{C}^{({\text{12}}\text{C}{\text{16}}\text{O})}$	+0.06	+0.04	-0.01	-0.03	—	0.00	-0.06	0.08	0.06
$\text{N}^{({\text{12}}\text{CN})}$	+0.04	+0.06	+0.00	+0.02	-0.27	—	+0.15	0.07	0.31
$\text{O}^{({\text{16}}\text{OH})}$	+0.08	+0.05	+0.02	+0.05	-0.06	-0.10	—	0.11	0.12
$^{12}\text{C}/^{13}\text{C}$	+1	-2	+2	+0	—	0	2	3	2
$^{16}\text{O}/^{17}\text{O}$	-40	-50	+10	-50	-10	+20	—	82	22
$^{16}\text{O}/^{18}\text{O}$	-100	+100	-100	0	-100	-100	—	173	141

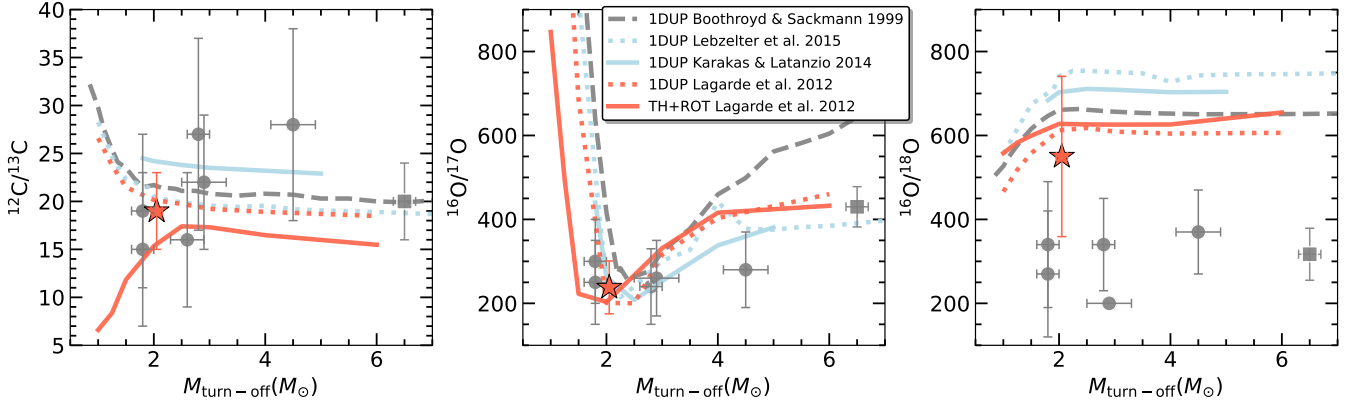


Figure 7. Carbon and oxygen isotopic ratios in the cluster NGC 5822 compared with mixing models and observational data from the literature. Predictions after the first dredge-up (1DUP) are shown from: Lebzelter et al. (2015, blue dotted lines), Karakas & Lattanzio (2014, blue solid lines), Lagarde et al. (2012, red dotted lines), and Boothroyd & Sackmann (1999, grey dashed lines). The thermohaline and rotation (TH+ROT) mixing model by Lagarde et al. (2012, red solid lines) is also presented. Grey circles represent stars analyzed by Lebzelter et al. (2015), and the grey square represents the open cluster NGC 2345 studied by Holanda et al. (2024a). The mean isotopic ratios and turn-off mass determined for NGC 5822 are represented by a red symbol.

Table 8. Comparison of projected rotational velocities ($v \sin i$) and lithium abundances between this work, Delgado Mena et al. (2016) (DM16), and Tsantaki et al. (2023) (TS23) for four stars in NGC 5822.

Star	$v \sin i$ (km s $^{-1}$)		$\log \varepsilon(\text{Li})_{\text{NLTE}}$		
	This Work	DM16	This Work	DM16	TS23
NGC 5822-001	4.70	—	0.24	—	0.13
NGC 5822-006	6.10	—	1.45	—	1.31
NGC 5822-008	5.00	3.79	0.67	0.80	0.43
NGC 5822-102	5.70	5.40	1.39	1.57	1.35
NGC 5822-201	4.70	4.17	0.83	1.18	1.01
NGC 5822-224	4.00	3.69	0.44	0.56	-0.11
NGC 5822-240	3.00	—	1.43	—	1.40
NGC 5822-316	3.00	—	0.98	—	0.64
NGC 5822-348	2.80	—	0.44	—	-0.22
NGC 5822-375	2.20	—	0.54	—	-0.08
NGC 5822-443	2.80	—	0.50	—	-0.14

Table 6). Nevertheless, the results obtained in our analysis are in excellent agreement with those of Tsantaki et al. (2023), especially for the Li-enriched stars. Larger differences arise for stars with very low Li abundances, which in most cases may be associated with uncertainties in the continuum placement or with the blending of CN and Fe lines near 6707.8 Å. Concerning the atmospheric parameters reported by Tsantaki et al. (2023), star #001 shows the most significant discrepancies, with $\Delta T_{\text{eff}} = 96$ K and $\Delta \log g = 0.40$ dex, while the remaining stars exhibit differences below 78 K and 0.17 dex, which are compatible with typical uncertainties in these parameters.

Isochrone fitting (Figure 1) indicates that the three Li-enriched

stars are likely in the red clump phase (core He-burning), the evolutionary stage most frequently associated with this type of peculiar star (Yan et al. 2021, among others). The most reliable method to determine whether Li-rich giants are on the RGB or in the red clump is asteroseismic data analysis, using the frequency of maximum oscillation power (ν_{max}) and the period spacing of gravity modes ($\Delta \Pi_1$) (e.g., Bedding et al. 2011; Mosser et al. 2014). In the absence of such data, particularly for stars in OCs, isochrone fitting provides a reasonable alternative for constraining the evolutionary stage. In this context, Delgado Mena et al. (2016) suggest that the giant stars analyzed (and with anomalous Li abundance) in NGC 5822 have undergone less lithium dilution because they are in an earlier phase of 1DUP. However, the authors assumes an age of 0.68 Gyr for the cluster (they plotted an isochrone 0.63–0.80 Gyr), based on the literature available, which differs significantly from more recent determinations (Table 2). On the other hand, Tsantaki et al. (2023) adopted the OC parameters from Bossini et al. (2019, 0.89 Gyr) and suggested that giants #006 and #102 could either be located at the base of the RGB or already lie in the red clump. For the star #240, the authors reported clear lithium enrichment based on its Li absorption line and proposed that it is positioned near the RGB tip. We reinforces the importance of a comprehensive analysis combining membership, accurate determination of cluster parameters, and chemical mixing indicators to better constrain the evolutionary stages of the stars. As said before, all stars analyzed in this work present C and N abundances compatible with post-1DUP chemical pattern.

Several scenarios have been proposed to explain the formation of Li-rich/enriched giant stars, but for the red clump stage, two main

mechanisms appear relevant to the stars analyzed in this work: mergers involving a helium white dwarf and an RGB star (e.g., [Zhang et al. 2020](#)) and helium-flash-induced mixing events ([Schwab 2020](#)). In the merger scenario, the final surface lithium abundance depends on the mass of the helium white dwarf. Models predict that mergers involving white dwarfs with masses between 0.35 and $0.40 M_{\odot}$ can produce Li-rich giants, while mergers outside this mass range are more likely to result in the formation of early-R type carbon stars. In the second scenario, the induced mixing is predicted to occur in low-mass stars after He flash and provides a single-star evolutionary pathway to explain Li enhancement in red clump giants, without requiring binary interaction.

3.1.2 Isotopic ratios

As already mentioned, isotopic ratios in atmospheres of red giant stars are known to be influenced by 1DUP, so they can serve as helpful probes to trace the induced envelope mixing in this kind of object (e.g., [Takeda et al. 2019](#)). In Figure 7 we compare observed $^{12}\text{C}/^{13}\text{C}$ and $^{16}\text{O}/^{17,18}\text{O}$ ratios in the NGC 5822 with mixing models, focusing on the effect of the 1DUP and extra mixing processes like thermohaline and rotation (TH+ROT) ([Boothroyd & Sackmann 1999](#); [Lebzelter et al. 2015](#); [Karakas & Lattanzio 2014](#); [Lagarde et al. 2012](#)). Additionally, isotopic ratio measurements from [Lebzelter et al. \(2015\)](#) and [Holanda et al. \(2024a\)](#) are included for comparison as gray circles and squares, respectively. The $^{12}\text{C}/^{13}\text{C}$ and $^{16}\text{O}/^{17}\text{O}$ ratios reveal a clear mass dependence: low-mass stars ($<2 M_{\odot}$) show significant change in these ratios after the 1DUP, and NGC 5822's results present a moderate agreement with predictions from both 1DUP and TH+ROT models. The two most evolved objects in the sample, stars #375 and #443, lie slightly above the red clump region and may already be evolving toward the early-AGB stage. Their $^{12}\text{C}/^{13}\text{C}$ ratios of 21 and 16, respectively, are consistent with expectations for post-1DUP giants that may already exhibit extra mixing. On the other hand, #240, which has just passed the RGB tip and is now approaching the red clump, is the least evolved star in the sample and shows the highest isotopic ratio, $^{12}\text{C}/^{13}\text{C}$ of 25. The remaining stars, all located within the red clump region (see Figure 1), present a broader range of isotopic ratios, from 12 to 24. Red clump stars may present different mixing histories depending on mass, rotation, and internal angular-momentum transport. In general, the distribution of $^{12}\text{C}/^{13}\text{C}$ values across the CMD is also in agreement with the expected evolutionary dependence of carbon isotopic ratios in low-mass giants.

A significant discrepancy is observed for the ^{18}O isotope, where the measured $^{16}\text{O}/^{18}\text{O}$ ratio significantly deviate from model predictions, mainly for the stars observed in the literature. As suggested by [Lebzelter et al. \(2015\)](#), this divergence may reflect uncertainties in the initial ^{18}O abundance or limitations in current nucleosynthetic yields and mixing prescriptions involving this isotope.

The TH+ROT models by [Lagarde et al. \(2012\)](#) predict more significant isotopic shifts compared to standard 1DUP models, particularly for carbon isotopic ratio, which is aligned with $[\text{Na}/\text{Fe}]$ ratio (see Section 3.3), suggesting that additional mixing mechanisms play a critical role in evolution of post-main-sequence stars.

3.2 Fluorine

In recent years, the number of notable NIR studies of OCs and field stars has been increasing, contributing to important discussions on Galactic fluorine (^{19}F) abundances ([Ryde et al. 2020](#); [Guerço et al.](#)

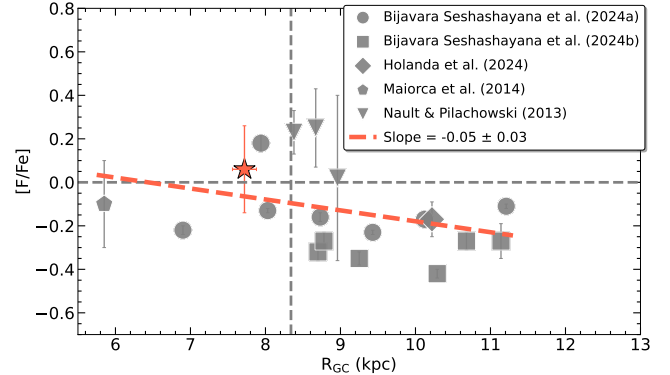


Figure 8. Galactocentric distance (R_{GC}) versus $[\text{F}/\text{Fe}]$ abundance for open clusters analyzed by [Bijavara Seshashayana et al. \(2024a\)](#) (circles), [Bijavara Seshashayana et al. \(2024b\)](#) (squares), [Holanda et al. \(2024\)](#) (diamond), [Maiorca et al. \(2014\)](#) (pentagons), and [Nault & Pilachowski \(2013\)](#) (triangles). The red dashed line shows the linear regression, while the vertical gray dashed line marks the solar Galactocentric distance (8.34 kpc; [Reid et al. 2014](#)). All fluorine abundance values are scaled to the solar reference by [Asplund et al. \(2009\)](#): $\log \varepsilon(\text{F}) = 4.56$.

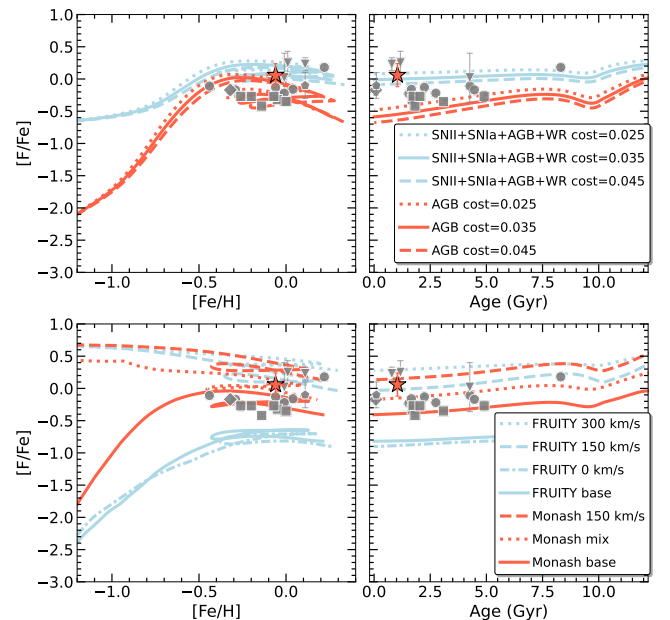


Figure 9. $[\text{Fe}/\text{H}]$ vs. $[\text{F}/\text{Fe}]$ and Age vs. $[\text{F}/\text{Fe}]$ for open clusters. The upper panels compare the observational data with predictions from the Galactic chemical evolution two infall model ([Spitoni et al. 2018](#)). The lower panels show comparisons with AGB nucleosynthesis models from the Monash and FRUITY grids. The symbols follow the same convention as in Figure 8.

2022; [Nandakumar et al. 2023](#); [Bijavara Seshashayana et al. 2024a,b](#); [Ryde et al. 2025](#)). [Clayton \(2003\)](#) suggested that approximately 15–30% of the Galactic fluorine abundance originates from He-burning shells in massive stars through the nuclear reaction $^{18}\text{O}(\text{p}, \gamma)^{19}\text{F}$. Beyond this, multiple production channels for fluorine have been discussed in the literature, including low-mass AGB stars, Wolf-Rayet stars (WR), Type Ia supernovae (SN Ia), and core-collapse supernovae (SN II), highlighting the complexity of the chemical evolution of fluorine in the Galaxy.

In Figure 8, we present the fluorine abundance gradient based on the NGC 5822 mean result along with OCs from the literature. The comparison includes results for NGC 6939, NGC 2420, NGC 7762, NGC 7142, Collinder 110, and Berkeley 32 from [Bijavara Seshashayana et al. \(2024b\)](#); NGC 7789, NGC 7044, NGC 6819, NGC 6791, Ruprecht 171, Trumpler 5, and King 11 from [Bijavara Seshashayana et al. \(2024a\)](#); NGC 2345 from [Holanda et al. \(2024a\)](#); NGC 6404 from [Maiorca et al. \(2014\)](#); and NGC 752, M 67, and Hyades from [Nault & Pilachowski \(2013\)](#). For this combined dataset, [Bijavara Seshashayana et al. \(2024b\)](#) reported a slope of $-0.09 \pm 0.02 \text{ dex kpc}^{-1}$ for the linear fit, which is consistent with our result of $-0.05 \pm 0.03 \text{ dex kpc}^{-1}$, within the uncertainties. These findings suggest a gradual decline in fluorine enrichment efficiency with increasing R_{GC} , likely reflecting radial variations in stellar populations and star formation history. NGC 5822 occupies an important position in the inner disk, where few clusters have available fluorine abundance measurements. Its well-determined distance and fluorine abundance help to partially fill the gap for OCs at $R_{\text{GC}} < 8 \text{ kpc}$, providing constraints for chemical evolution models. Moreover, the significant scatter among clusters at similar R_{GC} (8–9 kpc) underscores the importance of local astrophysical conditions in influencing fluorine production. An interesting case is presented by [Bijavara Seshashayana et al. \(2024a\)](#): the cluster NGC 6791, a metal-rich, fluorine-enhanced, and old OC, which is thought to have originated in the inner disk regions and later migrated outward, making it a notable outlier in the fluorine distribution.

In Figure 9, we compare the observational trends of [Fe/H] and Age versus [F/Fe], taking into account the same OCs from the literature, with predictions from three nucleosynthesis models: the two-infall Galactic chemical evolution model by [Spitoni et al. \(2019\)](#), and stellar yields from the Monash and the FULL-Network Repository of Updated Isotopic Tables & Yields (FRUITY) AGB nucleosynthesis models by [Lugaro et al. \(2012\)](#); [Fishlock et al. \(2014\)](#); [Karakas & Lugaro \(2016\)](#); [Karakas et al. \(2018\)](#) and [Cristallo et al. \(2009, 2011, 2015\)](#), respectively. A detailed description and discussion of these models are provided in [Bijavara Seshashayana et al. \(2024b\)](#). In the top panels, the two infall models incorporating all sources (SN II + SN Ia + AGB + WR; blue) predict higher [F/Fe] ratios at low [Fe/H] compared to AGB-only models (red), emphasizing the significant role of massive stars and supernovae in early fluorine enrichment. Additionally, given the uncertainties associated with the observed rates of SN Ia, different values for the model parameter were tested that governs the fraction of stellar systems capable of producing such supernovae. Following the same approach of [Bijavara Seshashayana et al. \(2024b\)](#), we considered three representative values: 0.025, 0.035, and 0.045. In terms of metallicity content, the NGC 5822 is in agreement with both models. On the other hand, only the models with all sources can fit NGC 5822 and other clusters with age less than 1.5–2.0 Gyr.

In the bottom panels of Figure 9, we compare predictions of [F/Fe] as functions of [Fe/H] and Age under different nucleosynthesis scenarios. For WR stars, we adopt the yield set of [Limongi & Chieffi \(2018\)](#), considering three rotational velocities: 0, 150, and 300 km s⁻¹. For low- and intermediate-mass stars, we test sets of yields from the FRUITY database and the Monash group. Our results indicate that fluorine yields from the Monash models are excellent to reproduce the observational data. Previous studies ([Prantzos et al. 2018](#); [Romano et al. 2019](#)) have suggested that in order to reproduce the observed abundance trends of several chemical elements in the Galaxy, massive stars must rotate more rapidly at low metallicities and more slowly at high metallicities. Motivated by this, we tested a mixed-rotation model (“Monash mix”), in which 80% of

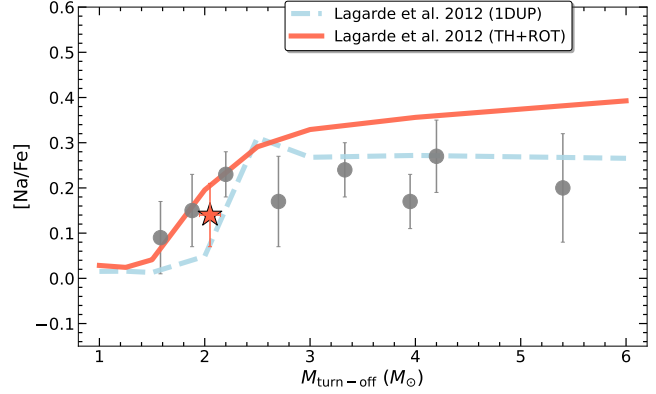


Figure 10. Turn-off mass versus [Na/Fe] ratio in giant stars of open clusters. We compare the mean result for the cluster NGC 5822 with open clusters previously studied by our team ([Katime Sanrich et al. 2013b](#); [Peña Suárez et al. 2018](#); [da Silveira et al. 2018](#); [Martínez et al. 2020](#); [Holanda et al. 2019, 2021, 2022](#)). Blue dashed line represents the predicted abundances of these elements for giants at the first dredge-up, using standard solar metallicity evolutionary models, and red solid line indicates prediction models for thermohaline and rotation-induced mixing from [Lagarde et al. \(2012\)](#).

low-metallicity massive stars are assumed to be fast rotators, while the remaining 20% are non-rotating. This model provides a better prediction to NGC 5822’s values and overall fit to the fluorine observations in [Fe/H] vs. [F/Fe] plot. We also note that average stellar rotational velocities are likely lower than 150 km s⁻¹, which may help explain the overproduction seen in models with 300 km s⁻¹ rotation rates.

The panel Age vs. [F/Fe] exhibits a clear dichotomy. The younger open clusters (< 2 Gyr) have the tendency to present higher values of [F/Fe] in relation to the older ones. This finding is consistent with the growing influence of AGB stars, which have been shown to enrich the interstellar medium in fluorine on timescales of up to several Gyr, depending on mass and metallicity. The fluorine produced in AGB stars is the result of helium burning and subsequent mixing processes, and their contribution becomes more prominent in later Galactic epochs. In contrast, older OCs, formed earlier in the Galaxy’s evolution, show systematically lower [F/Fe] values. These clusters are likely to reflect a chemical composition that has been imprinted by earlier generations of stars when fluorine production was primarily governed by massive stars and SN II. The negligible contribution of AGB stars to the fluorine budget in these populations lends further support to the time-delay scenario, wherein the accumulation of fluorine from AGB nucleosynthesis is a gradual process.

3.3 Odd-Z elements

Sodium (²³Na) is primarily produced during the carbon-burning phase in massive stars via the reaction ¹²C(¹²C, p)²³Na. Although part of the synthesized ²³Na is subsequently destroyed, a significant amount survives and is later ejected during SN II, which are the main contributors to Galactic sodium enrichment. Additional contributions arise from hydrogen-burning shells in evolved stars and, to a lesser extent, from the s-process via neutron capture on ²²Ne in AGB stars ([Clayton 2003](#)). The [Na/Fe] abundances obtained for the stars in NGC 5822 are in excellent agreement with the values reported by [Mishenina et al. \(2006\)](#) for clump giants. Moreover, when compared with theoretical models, the average Na abundance found

in our sample aligns well with the predictions from 1DUP and thermohaline plus rotational mixing models (TH+ROT) by [Lagarde et al. \(2012\)](#), as shown in Figure 10.

We did not detect any Na abundance enrichment in the Ba-stars, whose abundance values are consistent with those of typical red clump stars ($[\text{Na}/\text{Fe}] \sim 0.05\text{--}0.15$ dex). An enhancement in this chemical specie in Ba-stars may be associated with pollution by AGB companions with mass $M \geq 4.0 M_{\odot}$. This result helps to better constrain the mass of the AGB companions of these stars, as discussed in Section 3.6.1.

The nucleosynthesis of aluminum, ^{27}Al , is also primarily associated with the evolution of massive stars. As a result, aluminum abundances in stellar populations can serve as effective tracers of SN II. In Figure 3, the $[\text{Al}/\text{Fe}]$ ratios exhibit excellent agreement with those stars of similar metallicity analyzed by [Bensby et al. \(2014\)](#), showing no signs of enrichment and showing only a small dispersion for the stars in NGC 5822.

Phosphorus nucleosynthesis derives almost entirely from neon-burning, which occurs at the end of carbon-burning in massive stars ([Clayton 2003](#)). In Figure 3, P abundances are in good agreement with the literature results ([Nandakumar et al. 2022](#)), though it exhibits a notable dispersion among the cluster stars. This internal dispersion in OC's results may be attributed to the influence of spectral line blending with CO lines in the abundance determination in 16483 Å (see Figure 2).

3.4 Alpha elements

The α -to-iron abundance ratio (α/Fe) can serve as an indirect method for estimating stellar ages. This is because α -elements such as Mg, Si, S, Ca, and Ti are rapidly produced by SN II, whereas iron is synthesized over longer timescales through SN Ia ([Kobayashi et al. 2020](#)).

The Mg abundances derived by [Mishenina et al. \(2006\)](#) show good agreement with the values obtained for the analyzed stars in NGC 5822. Again, the star #001, a probable non-member of the cluster, displays the largest deviation from the OC's mean Mg abundance, which is $\langle [\text{Mg}/\text{Fe}] \rangle = +0.01$ dex. When comparing our abundance results with the dwarf stars analyzed by [Bensby et al. \(2014\)](#), we find excellent agreement for Si and Ca. Ti abundances are subsolar and relatively low at a metallicity of $[\text{Fe}/\text{H}] = -0.06$ dex, a trend also observed in the comparison with field stars. Although the differences are small and consistent with the uncertainties, a similar behavior is reported by [Ramos et al. \(2024\)](#) and [Alonso-Santiago et al. \(2020\)](#) for the cluster NGC 6664.

Sulfur abundances are compared with those of 30 dwarf stars analyzed by [Lucertini et al. \(2022\)](#). While their results include NLTE corrections, the S I multiplet at 6757 Å used in our analysis of NGC 5822 exhibits negligible departures from LTE (e.g., [Takeda et al. 2005](#)), making our LTE results reliable for this comparison. This reliability is further supported by the good agreement observed between the two samples at similar metallicities, as shown in Figure 3.

3.5 Iron-peak elements

Approximately half of the iron-peak elements are produced in the evolution of low- and intermediate mass stars in binary systems, such as in SN Ia, reflecting their prolonged enrichment timescale. However, these elements can also be synthesized through incomplete or complete silicon-burning during SN II ([Kobayashi et al. 2020](#), and references therein).

All neutral species analyzed in this work exhibit measurable lines in both optical and NIR spectral domains. The abundance results show excellent agreement between the optical and NIR analyses, with the largest discrepancy observed between Sc II (optical) and Sc I (NIR); however, within the uncertainties, there is agreement. When comparing the abundance results for NGC 5822 with those of dwarf stars from [Bensby et al. \(2014\)](#) and [Battistini & Bensby \(2015\)](#), we find good agreement across all analyzed species. Concerning Cr abundances, all individual values are consistent with those reported for dwarf stars in [Bensby et al. \(2014\)](#), when considering the associated uncertainty for this element.

3.6 s- and r-process elements

Elements heavier than iron-peak elements ($Z > 30$) are primarily synthesized through neutron-capture processes, with only a minor contribution from proton-rich nuclei produced via photodisintegration. These processes are classified as either slow (s-process) or rapid (r-process), depending on whether the neutron-capture timescale is longer or shorter than the β -decay timescale of unstable isotopes (see [Lugaro et al. 2023](#)). The s-process occurs mainly in low- and intermediate mass AGB stars ([Burbidge et al. 1957; Busso et al. 1999](#)) and accounts for 71.9 %, 83.5 %, 57.5 %, 40.5 %, and 87.2 % of the solar system abundances of Y, Ce, Nd, Yb, and Pb, respectively ([Bisterzo et al. 2014](#)). With the exception of Yb, all heavy elements analyzed in this work are classified as s-process elements.

The normal stars (in terms of s-process species) in our sample exhibit s-process element abundances in close agreement with the Y and Yb abundance values reported in the literature ([Battistini & Bensby 2016; Montelius et al. 2022](#)). The ytterbium results are exclusively obtained from the NIR analysis, while yttrium results are a mean of optical and NIR results. However, Ce and Nd abundances appear slightly enriched, a trend observed in both optical and NIR results, with a small mean dispersion for both species (Table 4). In [Bijavara Seshashayana et al. \(2024a\)](#), the authors investigate a possible connection between fluorine F and Ce abundances, considering factors such as metallicity, age, and Galactocentric distance, given that both elements are produced in AGB stars. In the stellar context, as previously noted, HF lines are not detectable in either of the Ba-stars due to their high effective temperatures. Also, any potential fluorine enrichment in their atmospheres could not be confirmed.

Pb abundances present significant dispersion for the OC mean value, likely due to the uncertainty of continuum determination – Pb $\lambda 4057$ Å is in a region of many blending for the interval of metallicity and temperature of the sample analyzed here. This spread is also observed in the literature results by [Contursi et al. \(2024\)](#). Additionally, NLTE corrections in Pb results are in excellent agreement with the values reported by [Contursi et al. \(2024\)](#), who also provide NLTE Pb results.

Star #001 stands out by exhibiting the lowest abundances of Y, Ce, and Nd in the sample, reinforcing the same trend of deficiency observed in other elements previously discussed.

3.6.1 The barium stars

The two Ba-stars in our sample, #002 and #201, exhibit all the typical characteristics of this class: moderate to high enrichment in heavy elements such as Y, Ce, Nd and Yb, and slight enrichment in ^{12}C . As previously mentioned, both stars also show elevated RUWE values, suggesting binarity and complicating astrometric membership assessment. Nevertheless, for elements not affected by binary mass

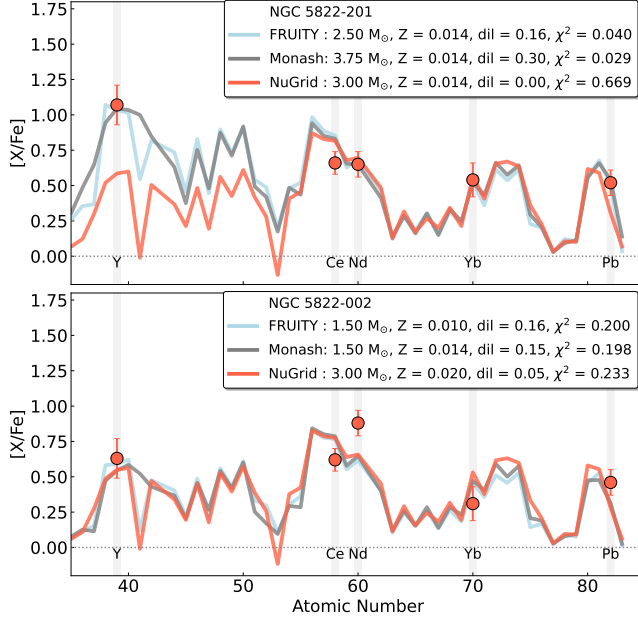


Figure 11. Comparison between the observed chemical abundances (red circles) and predictions from the FRUITY (blue), Monash (gray), and NuGrid (red) nucleosynthesis models, each assuming different stellar masses. The metallicity (Z), dilution factor (dil), and χ^2 value for each model are also indicated.

transfer, their abundances are consistent with those of confirmed cluster members.

Keeping this in mind, we explore here the abundances of five heavy elements observed in the Ba-stars #002 and #201, in light of the Monash, FRUITY, and NuGrid (Battino et al. 2019) s -process nucleosynthesis models. Together, the Monash and FRUITY models cover a wide range of stellar masses ($1.0 - 8.0 M_{\odot}$) and metallicities ($-1.20 \leq [\text{Fe}/\text{H}] \leq +0.30$). On the other hand, NuGrid models are available for 2 and $3 M_{\odot}$, close to solar metallicity ($[\text{Fe}/\text{H}] \approx -0.15, +0.16$, and $+0.30$), and include convective boundary mixing (CBM) at the bottom of the He intershell during the thermal pulse episodes.

The abundance patterns of the neutron-capture elements observed in #002 and #201 were compared with predictions from these three sets of nucleosynthesis models. To carry out this task, we followed the same approach as Roriz et al. (2024), by applying dilution to the models and searching for the best fits between observation and predictions, allowing us to find constraints on mass of the polluter TP-AGB stars. The elemental abundances, which probe the three peaks of the s -process, as well as the region between the second and third peaks, together with the theoretical predictions are shown in Figure 11. In general, low-mass models are able to reproduce the observations, in agreement with other studies (e.g. Cseh et al. 2022). For AGB stars in this mass range, the initial–final mass relation of El-Badry et al. (2018) predicts white dwarf progeny masses $\lesssim 0.7 M_{\odot}$. This is further supported by the low values of the mass function derived for Ba stars; for the star #002, Van der Swaelmen et al. (2017) reported $f(m) = 0.009 M_{\odot}$. Such a low value points out for a white dwarf as the unseen companion of #002, which is expected as the final remnant of a former low-mass polluter TP-AGB stars. For the star #201, in particular, a Monash model of $3.75 M_{\odot}$ accompanied by the largest dilution factor (dil = 0.30) is need to fit the observations. This mass value is aligned with no sodium enrichment which is related to

scenario of intermediate-low-mass polluting AGB. Interestingly, the NuGrid models that best fit the profiles observed in #002 and #201 are those labeled “h-CBM”, which produce larger ^{13}C -pockets; these, in turn, needed of lower dilutions (dil $\simeq 0.00$). However, the NuGrid model does not reach the level of the [Y/Fe] ratio observed for #201, unlike the Monash and FRUITY models which closely reproduce it. As far as the second peak is concerned, all the models overproduce Ce in both stars. Finally, in light of Yb abundances in #002 and #201, there does not appear to be additional contribution from another nucleosynthetic source, in addition to s -process.

The presence of the Ba-star #002, apparently polluted by a $\sim 1.5 M_{\odot}$ AGB companion according to the Monash and FRUITY models, appears at first glance to be inconsistent with the OC’s turn-off mass ($2.05 M_{\odot}$). The AGBS’s mass of $1.5 M_{\odot}$ estimate from nucleosynthesis models is subject to significant uncertainties, particularly due to the complex dependence of s -process yields on stellar parameters such as metallicity, mixing efficiency, and the formation of the ^{13}C pocket. In this context, although it results in a higher χ^2 value, the NuGrid model yielding a $3.0 M_{\odot}$ TP-AGB polluter suggests a more plausible mass for the AGB companion.

4 CONCLUSION

In this work, we present a comprehensive chemical analysis of thirteen red giant stars in the open cluster NGC 5822. The study is based on high-resolution spectra obtained with two different spectrographs, FEROS and IGRINS, covering optical and near-infrared wavelengths (H and K bands). For the first time, we provide abundances of F, P, K, and Yb, as well as $^{17}\text{O}/^{16}\text{O}$ and $^{18}\text{O}/^{16}\text{O}$ isotopic ratios for stars in this well-studied cluster. We also performed an independent membership analysis using astrometric data from the Gaia mission. Three stars were removed from this astrometric analysis due to high RUWE values (#001, #002, and #201), but two of them are in binary systems and have been classified as Ba-stars (#002 and #201). The Ba-stars present chemical pattern compatible with the members of the cluster, while the star #001 differ significantly.

The membership results and physical parameters derived for the cluster, such as age, distance, reddening, and mean astrometric values, are consistent with those reported in the literature (Cantat-Gaudin et al. 2020; Dias et al. 2021; Hunt & Reffert 2023), validating the robustness of our membership determination. Based on these primary parameters, additional quantities were calculated, including the turn-off mass and the Galactocentric distance. These values are fundamental for interpreting the chemical abundance results within the broader context of stellar and galactic chemical evolution. First, the turn-off mass was used to test mixing models for Na, $^{12}\text{C}/^{13}\text{C}$, $^{16}\text{O}/^{17}\text{O}$, and $^{16}\text{O}/^{18}\text{O}$ isotopic ratios, as well as to constrain AGB nucleosynthesis models. All evolutionary models are very sensitive to stellar mass, particularly near the critical threshold of $2.0 M_{\odot}$, which is very close to the turn-off mass of NGC 5822 ($2.05 M_{\odot}$). We find agreement with the predictions of 1DUP and thermohaline mixing from Lagarde et al. (2012) in the $^{12}\text{C}/^{13}\text{C}$ ratios. The observed spread, from 12 to 25, reflects differences in evolutionary stage, as well as additional factors such as mass, rotation, and internal angular-momentum transport. Regarding the AGB nucleosynthesis models used to estimate the mass of the polluting companion in Ba-stars, the turn-off mass allowed us to rule out $1.5 M_{\odot}$ models, even in the case of star #002, where such models yielded a lower χ^2 . The absence of Na enrichment in the Ba-stars led us to associate $4.0 M_{\odot}$ as an upper limit for the mass of the AGB polluting companions.

This is consistent with the derived values of 3.00 and $3.75 M_{\odot}$ for stars #002 and #201, respectively.

The Li-enriched stars #006, #102, and #240 do not exhibit any anomalous chemical abundances or isotopic ratios that could be linked to a specific Li enrichment scenario. However, isochrone fitting indicates that their most probable evolutionary stage is the red clump, which is consistent with the phase most commonly associated with Li-rich/enriched giant stars (Yan et al. 2021, among others). In the absence of asteroseismic data the isochrone fitting serves as a reliable alternative and represents an advantage when analyzing peculiar stars in open clusters. Based on their evolutionary stage, the candidate mechanisms to explain the formation of these stars include a merger event involving a helium white dwarf ($0.35 \leq M/M_{\odot} \leq 0.40$) and a RGB star (Zhang et al. 2020), as well as the helium-flash-induced mixing scenario (Schwab 2020). The analysis of the Ca II H & K lines indicates the presence of chromospheric activity in stars #006 and #102. Although stellar activity is often discussed in connection with enhanced lithium abundances, rapid rotation, or binarity, these stars do not exhibit high projected rotational velocities ($v \sin i \gtrsim 8 \text{ km s}^{-1}$) nor any evidence of binarity, suggesting that activity alone is not sufficient to explain their lithium enrichment.

A Galactic gradient of fluorine was derived by combining results from the literature. We obtained a slope of $-0.05 \pm 0.03 \text{ dex kpc}^{-1}$ for the inner disk. Our result is consistent with the slope of $-0.09 \pm 0.02 \text{ dex kpc}^{-1}$ reported by Bijavara Seshashayana et al. (2024b), although we emphasize the scarcity of open clusters with Galactocentric distances $\leq 8.0 \text{ kpc}$ in the current sample. The results of fluorine nucleosynthesis models indicate a composite origin for fluorine, with early rapid enrichment by massive stars followed by a more extended and metallicity-dependent contribution from AGB stars. Fluorine in Ba-stars may be enriched since AGB stars are an important astrophysical site of this species. However, even with probable enrichment, the effective temperature values observed in the stars #002 and #201 make this analysis impossible. In this context, a near-infrared study of cool field Ba-stars is currently being prepared by our group.

ACKNOWLEDGMENTS

NH thanks Chessy for all the technical support. The authors acknowledge Lyudmila Mashonkina for providing the NLTE corrections for the Pb abundances. We also thank Donatella Romano and Emanuele Spitoni for kindly sharing their model prediction files. The authors are grateful to Jane Gregorio-Hetem for reading the manuscript and providing helpful suggestions. This work has been developed under a fellowship of the Fundação de Amparo à Pesquisa do Estado do Rio de Janeiro – FAPERJ, Rio de Janeiro, Brazil, grant E-26/200.097/2025. V.L.T. acknowledges a fellowship 302195/2024-6 of the PCI Program – MCTI and a fellowship 152242/2024-4 of the PDJ – MCTI and CNPq. S.B.S. acknowledges funding from the Crafoord Foundation. M.P.R. acknowledges financial support from the Coordenação de Aperfeiçoamento de Pessoal de Nível Superior – Brasil (CAPES) – Finance Code 001. M.B.F. acknowledges financial support from the National Council for Scientific and Technological Development (CNPq), Brazil (grant number 307711/2022-6). C.M. acknowledges financial support from the Consejo Nacional de Investigaciones Científicas y Técnicas (CONICET). S.D. acknowledges CNPq/MCTI for grant 306859/2022-0 and FAPERJ for grant 210.688/2024.

This work used the Immersion Grating Infrared Spectrometer (IGRINS) that was developed under a collaboration between the

University of Texas at Austin and the Korea Astronomy and Space Science Institute (KASI) with the financial support of the Mt. Cuba Astronomical Foundation, of the US National Science Foundation under grants AST-1229522 and AST-1702267, McDonald Observatory of the University of Texas at Austin, of the Korean GMT Project of KASI, and Gemini Observatory.

DATA AVAILABILITY

Data are available on request. The data underlying this article will be shared on reasonable request to the corresponding author.

REFERENCES

Afşar M., et al., 2018, *ApJ*, **865**, 44
 Alonso-Santiago J., Negueruela I., Marco A., Tabernero H. M., Castro N., 2020, *A&A*, **644**, A136
 Alonso A., Arribas S., Martínez-Roger C., 1999, *A&AS*, **140**, 261
 Asplund M., Grevesse N., Sauval A. J., Scott P., 2009, *ARA&A*, **47**, 481
 Battino U., et al., 2019, *MNRAS*, **489**, 1082
 Battistini C., Bensby T., 2015, *A&A*, **577**, A9
 Battistini C., Bensby T., 2016, *A&A*, **586**, A49
 Bedding T. R., et al., 2011, *Nature*, **471**, 608
 Bensby T., Feltzing S., Oey M. S., 2014, *A&A*, **562**, A71
 Bijavara Seshashayana S., et al., 2024a, *A&A*, **683**, A218
 Bijavara Seshashayana S., et al., 2024b, *A&A*, **689**, A120
 Bisterzo S., Travaglio C., Gallino R., Wiescher M., Käppeler F., 2014, *ApJ*, **787**, 10
 Böcek Topcu G., et al., 2019, *MNRAS*, **485**, 4625
 Böcek Topcu G., et al., 2020, *MNRAS*, **491**, 544
 Boothroyd A. I., Sackmann I. J., 1999, *ApJ*, **510**, 232
 Bossini D., et al., 2019, *A&A*, **623**, A108
 Bressan A., Marigo P., Girardi L., Salasnich B., Dal Cero C., Rubele S., Nanni A., 2012, *MNRAS*, **427**, 127
 Brooke J. S., Bernath P. F., Western C. M., Sneden C., Afşar M., Li G., Gordon I. E., 2016, *JQSRT*, **168**, 142
 Brown J. A., Sneden C., Lambert D. L., Dutchover Edward J., 1989, *ApJS*, **71**, 293
 Burbidge E. M., Burbidge G. R., Fowler W. A., Hoyle F., 1957, *Reviews of Modern Physics*, **29**, 547
 Busso M., Gallino R., Wasserburg G. J., 1999, *ARA&A*, **37**, 239
 Cantat-Gaudin T., et al., 2020, *A&A*, **640**, A1
 Casali G., et al., 2019, *A&A*, **629**, A62
 Castelli F., Kurucz R. L., 2004, arXiv preprint astro-ph/0405087
 Chaboyer B., Demarque P., Kernan P. J., Krauss L. M., 1998, *ApJ*, **494**, 96
 Civisić S., Ferus M., Chernov V. E., Zanozina E. M., 2013, *A&A*, **554**, A24
 Clayton D., 2003, *Handbook of Isotopes in the Cosmos*. Cambridge, UK: Cambridge University Press
 Contursi G., de Laverny P., Recio-Blanco A., Molero M., Spitoni E., Matteucci F., Cristallo S., 2024, *A&A*, **690**, A97
 Cox A. N., 2000, *Allen's astrophysical quantities*. Springer Science & Business Media
 Cristallo S., Straniero O., Gallino R., Piersanti L., Domínguez I., Lederer M. T., 2009, *ApJ*, **696**, 797
 Cristallo S., et al., 2011, *ApJS*, **197**, 17
 Cristallo S., Straniero O., Piersanti L., Gobrecht D., 2015, *ApJS*, **219**, 40
 Cseh B., et al., 2022, *A&A*, **660**, A128
 Cunha K., et al., 2017, *ApJ*, **844**, 145
 Davis S. P., Phillips J. G., 1963, The red system (A2[pi]-X2[Sigma]) of the CN molecule. Univ. California Press
 Delgado Mena E., et al., 2016, *A&A*, **587**, A66
 Dias W. S., Monteiro H., Moitinho A., Lépine J. R. D., Carraro G., Paunzen E., Alessi B., Villegas L., 2021, *MNRAS*, **504**, 356
 Donor J., et al., 2020, *AJ*, **159**, 199
 Drake N. A., de la Reza R., da Silva L., Lambert D. L., 2002, *AJ*, **123**, 2703

El-Badry K., Rix H.-W., Weisz D. R., 2018, *ApJ*, **860**, L17

Fekel F. C., 1997, *PASP*, **109**, 514

Fekel F. C., Henry G. W., 2005, *AJ*, **129**, 1669

Fekel F. C., Henry G. W., Eaton J. A., Sperauskas J., Hall D. S., 2002, *AJ*, **124**, 1064

Fishlock C. K., Karakas A. I., Lugaro M., Yong D., 2014, *ApJ*, **797**, 44

Flaughabe T., et al., 2025, arXiv e-prints, p. arXiv:2512.16042

Gaia Collaboration et al., 2023, *A&A*, **674**, A1

Gonçalves B. F. O., da Costa J. S., de Almeida L., Castro M., do Nascimento Jr. J.-D., 2020, *MNRAS*, **498**, 2295

Goorvitch D., 1994, *ApJS*, **95**, 535

Guerço R., et al., 2022, *MNRAS*, **516**, 2801

Hasselquist S., et al., 2016, *ApJ*, **833**, 81

Hernandez X., Verteletskyi V., Nasser L., Aguayo-Ortiz A., 2024, *MNRAS*, **528**, 4720

Hobbs L. M., Thorburn J. A., Rebull L. M., 1999, *ApJ*, **523**, 797

Holanda N., Pereira C. B., Drake N. A., 2019, *MNRAS*, **482**, 5275

Holanda N., Drake N. A., Pereira C. B., 2020a, *MNRAS*,

Holanda N., Drake N. A., Pereira C. B., 2020b, *AJ*, **159**, 9

Holanda N., Drake N. A., Corradi W. J. B., Ferreira F. A., Maia F., Magrini L., da Silva J. R. P., Pereira C. B., 2021, *MNRAS*, **508**, 5786

Holanda N., Ramos A. A., Peña Suárez V. J., Martinez C. F., Pereira C. B., 2022, *MNRAS*, **516**, 4484

Holanda N., Drake N. A., Pereira C. B., 2023, *MNRAS*, **518**, 4038

Holanda N., Roriz M. P., Drake N. A., Junqueira S., Daflon S., da Silva J. R. P., Pereira C. B., 2024a, *MNRAS*, **527**, 1389

Holanda N., Flaughabe T., Quispe-Huaynasi F., Sonally A., Pereira C. B., 2024b, *ApJ*, **971**, 152

Huber K., Herzberg G., 1979, Molecular Spectra and Molecular Structure. New York, USA: Van Nostrand Reinhold Company

Hunt E. L., Reffert S., 2023, *A&A*, **673**, A114

Jönsson H., et al., 2014, *A&A*, **564**, A122

Karakas A. I., Lattanzio J. C., 2014, *Publ. Astron. Soc. Australia*, **31**, e030

Karakas A. I., Lugaro M., 2016, *ApJ*, **825**, 26

Karakas A. I., Lugaro M., Carlos M., Cseh B., Kamath D., García-Hernández D. A., 2018, *MNRAS*, **477**, 421

Katime Santrich O. J., Pereira C. B., de Castro D. B., 2013a, *AJ*, **146**, 39

Katime Santrich O. J., Pereira C. B., Drake N. A., 2013b, *A&A*, **554**, A2

Katime Santrich O. J., Kerber L., Abuchaim Y., Gonçalves G., 2022, *MNRAS*, **514**, 4816

Kaufer A., Stahl O., Tubbesing S., Nørregaard P., Avila G., Francois P., Pasquini L., Pizzella A., 1999, *The Messenger*, **95**, 8

Kobayashi C., Karakas A. I., Lugaro M., 2020, *ApJ*, **900**, 179

Kramida A., Ralchenko Y., Reader J., et al., 2014, URL <https://physics.nist.gov/asd>

Krolikowski D. M., Kraus A. L., Rizzuto A. C., 2021, *AJ*, **162**, 110

Krone-Martins A., Moitinho A., 2014, *A&A*, **561**, A57

Kumar Y. B., Reddy B. E., Lambert D. L., 2011, *ApJ*, **730**, L12

Kurucz R. L., 2011, *Canadian Journal of Physics*, **89**, 417

Lagarde N., Decressin T., Charbonnel C., Eggenberger P., Ekström S., Palacios A., 2012, *A&A*, **543**, A108

Lambert D. L., 1978, *MNRAS*, **182**, 249

Lambert D. L., Heath J. E., Lemke M., Drake J., 1996, *ApJS*, **103**, 183

Lebzelter T., Straniero O., Hinkle K. H., Nowotny W., Aringer B., 2015, *A&A*, **578**, A33

Limongi M., Chieffi A., 2018, *ApJS*, **237**, 13

Lind K., Asplund M., Barklem P. S., 2009, *A&A*, **503**, 541

Lind K., Asplund M., Barklem P. S., Belyaev A. K., 2011, *A&A*, **528**, A103

Lindgren L., et al., 2021, *A&A*, **649**, A2

Lucertini F., Monaco L., Caffau E., Bonifacio P., Mucciarelli A., 2022, *A&A*, **657**, A29

Lugaro M., Karakas A. I., Stancliffe R. J., Rijs C., 2012, *ApJ*, **747**, 2

Lugaro M., Pignatari M., Reifarth R., Wiescher M., 2023, *Annual Review of Nuclear and Particle Science*, **73**, 315

Magrini L., et al., 2021, *A&A*, **651**, A84

Maiorca E., Uitenbroek H., Utenthaler S., Randich S., Busso M., Magrini L., 2014, *ApJ*, **788**, 149

Majewski S. R., et al., 2017, *AJ*, **154**, 94

Martell S. L., et al., 2021, *MNRAS*, **505**, 5340

Martinez C. F., Holanda N., Pereira C. B., Drake N. A., 2020, *MNRAS*, **494**, 1470

Mashonkina L., Ryabtsev A., Frebel A., 2012, *A&A*, **540**, A98

McClure R. D., 1983, *ApJ*, **268**, 264

Mermilliod J. C., Mayor M., Udry S., 2008, *A&A*, **485**, 303

Mishenina T. V., Bienaymé O., Gorbaneva T. I., Charbonnel C., Soubiran C., Korotin S. A., Kovtyukh V. V., 2006, *A&A*, **456**, 1109

Montelius M., et al., 2022, *A&A*, **665**, A135

Morel T., Micela G., Favata F., Katz D., 2004, *A&A*, **426**, 1007

Mosser B., et al., 2014, *A&A*, **572**, L5

Myers N., et al., 2022, *AJ*, **164**, 85

Nandakumar G., Ryde N., Montelius M., Thorsbro B., Jönsson H., Mace G., 2022, *A&A*, **668**, A88

Nandakumar G., Ryde N., Mace G., 2023, arXiv e-prints, p. arXiv:2306.08446

Nandakumar G., Ryde N., Hartman H., Mace G., 2024, *A&A*, **690**, A226

Nandakumar G., Ryde N., Schultheis M., Rich R. M., di Matteo P., Thorsbro B., Mace G., 2025, *ApJ*, **982**, L14

Nault K. A., Pilachowski C. A., 2013, *AJ*, **146**, 153

Nine A. C., Mathieu R. D., Schuler S. C., Milliman K. E., 2024, *ApJ*, **970**, 187

Nordlander T., Lind K., 2017, *A&A*, **607**, A75

Osorio Y., Barklem P. S., Lind K., Belyaev A. K., Spielfiedel A., Guitou M., Feautrier N., 2015, *A&A*, **579**, A53

Pace G., Danziger J., Carraro G., Melendez J., François P., Matteucci F., Santos N. C., 2010, *A&A*, **515**, A28

Pal H., Subramaniam A., Reddy A. B. S., Jadhav V. V., 2024, *ApJ*, **970**, L39

Peña Suárez V. J., Sales Silva J. V., Katime Santrich O. J., Drake N. A., Pereira C. B., 2018, *ApJ*, **854**, 184

Pehlivan A., Nilsson H., Hartman H., 2015, *A&A*, **582**, A98

Pera M. S., Perren G. I., Moitinho A., Navone H. D., Vazquez R. A., 2021, *A&A*, **650**, A109

Perren G. I., Vázquez R. A., Piatti A. E., 2015, *A&A*, **576**, A6

Placco V. M., Sneden C., Roederer I. U., Lawler J. E., Den Hartog E. A., Hejazi N., Maas Z., Bernath P., 2021, *Research Notes of the American Astronomical Society*, **5**, 92

Prantzos N., Abia C., Limongi M., Chieffi A., Cristallo S., 2018, *MNRAS*, **476**, 3432

Ramos A. A., Holanda N., Drake N. A., Rain M. J., Maia F. F. S., Daflon S., Pereira C. B., 2024, *MNRAS*, **527**, 6211

Randich S., et al., 2022, *A&A*, **666**, A121

Rebolo R., Beckman J. E., 1988, *A&A*, **201**, 267

Reid M. J., et al., 2014, *ApJ*, **783**, 130

Rolo I., Delgado Mena E., Tsantaki M., Gomes da Silva J., 2024, *A&A*, **688**, A68

Romano D., Matteucci F., Zhang Z.-Y., Ivison R. J., Ventura P., 2019, *MNRAS*, **490**, 2838

Roriz M. P., Holanda N., da Conceição L. V., Junqueira S., Drake N. A., Sonally A., Pereira C. B., 2024, *AJ*, **167**, 184

Ryde N., et al., 2020, *ApJ*, **893**, 37

Ryde N., et al., 2025, *ApJ*, **979**, 174

Sales Silva J. V., Peña Suárez V. J., Katime Santrich O. J., Pereira C. B., Drake N. A., Roig F., 2014, *AJ*, **148**, 83

Sales-Silva J. V., et al., 2022, *ApJ*, **926**, 154

Schwab J., 2020, *ApJ*, **901**, L18

Skumanich A., 1972, *ApJ*, **171**, 565

Smith V. V., Lambert D. L., Nissen P. E., 1998, *ApJ*, **506**, 405

Smith V. V., et al., 2013, *ApJ*, **765**, 16

Sneden C. A., 1973, PhD thesis, THE UNIVERSITY OF TEXAS AT AUSTIN.

Sneden C., Lambert D. L., 1982, *ApJ*, **259**, 381

Sneden C., Lucatello S., Ram R. S., Brooke J. S. A., Bernath P., 2014, *ApJS*, **214**, 26

Sneden C., et al., 2022, *ApJ*, **940**, 12

Sousa S. G., Santos N. C., Adibekyan V., Delgado-Mena E., Israeli G., 2015, *A&A*, **577**, A67

Spitoni E., Matteucci F., Jönsson H., Ryde N., Romano D., 2018, *A&A*, **612**, A16

Spitoni E., Silva Aguirre V., Matteucci F., Calura F., Grisoni V., 2019, *A&A*, **623**, A60

Takeda Y., Tajitsu A., 2017, *PASJ*, **69**, 74

Takeda Y., Hashimoto O., Taguchi H., Yoshioka K., Takada-Hidai M., Saito Y., Honda S., 2005, *PASJ*, **57**, 751

Takeda Y., Omiya M., Harakawa H., Sato B., 2019, *PASJ*, **71**, 119

Tody D., 1986, in Crawford D. L., ed, Society of Photo-Optical Instrumentation Engineers (SPIE) Conference Series Vol. 627, Instrumentation in astronomy VI. p. 733, doi:10.1117/12.968154

Tsantaki M., Delgado-Mena E., Bossini D., Sousa S. G., Pancino E., Martins J. H. C., 2023, arXiv e-prints, p. arXiv:2303.16124

Van der Swaelmen M., Boffin H. M. J., Jorissen A., Van Eck S., 2017, *A&A*, **597**, A68

Viscasillas Vázquez C., et al., 2022, *A&A*, **660**, A135

Wilson O. C., Skumanich A., 1964, *ApJ*, **140**, 1401

Wyller A. A., 1966, *ApJ*, **143**, 828

Xing L.-F., Li Y.-C., Chang L., Wang C.-J., Bai J.-M., 2021, *A&A*, **653**, A28

Yan H.-L., et al., 2021, *Nature Astronomy*, **5**, 86

Yuk I.-S., et al., 2010, in McLean I. S., Ramsay S. K., Takami H., eds, Society of Photo-Optical Instrumentation Engineers (SPIE) Conference Series Vol. 7735, Ground-based and Airborne Instrumentation for Astronomy III. p. 77351M, doi:10.1117/12.856864

Zhang X., Jeffery C. S., Li Y., Bi S., 2020, *ApJ*, **889**, 33

da Silveira M. D., Pereira C. B., Drake N. A., 2018, *MNRAS*, **476**, 4907

This paper has been typeset from a $\text{\TeX}/\text{\LaTeX}$ file prepared by the author.